

PAPER

## Overview of verification tests on AC loss, contact resistance and mechanical properties of ITER conductors with transverse loading up to 30 000 cycles

To cite this article: K A Yagotintsev *et al* 2019 *Supercond. Sci. Technol.* **32** 105015

View the [article online](#) for updates and enhancements.





**IOP | ebooks™**

Bringing you innovative digital publishing with leading voices to create your essential collection of books in STEM research.

Start exploring the collection - download the first chapter of every title for free.

# Overview of verification tests on AC loss, contact resistance and mechanical properties of ITER conductors with transverse loading up to 30000 cycles

K A Yagotintsev<sup>1</sup> , W A J Wessel<sup>1</sup>, A Vostner<sup>2</sup>, A Devred<sup>2</sup>, D Bessette<sup>2</sup>, N Mitchell<sup>2</sup>, Y Nabara<sup>3</sup>, T Boutboul<sup>4</sup>, V Tronza<sup>5</sup>, S-H Park<sup>6</sup>, W Yu<sup>7</sup>, N Martovetsky<sup>8</sup> and A Nijhuis<sup>1</sup> 

<sup>1</sup> University of Twente, Faculty of Science & Technology, 7522 NB Enschede, The Netherlands

<sup>2</sup> ITER International Organization, Route de Vinon-sur-Verdon, F-13115 Saint-Paul-lez-Durance, France

<sup>3</sup> National Institute for Quantum and Radiological Science and Technology, 801-1, Muko-yama, Naka-shi, Ibaraki, 311-0193 Japan

<sup>4</sup> Fusion for Energy (F4E), ITER Department. Magnet Project Team, E-08019 Barcelona, Spain

<sup>5</sup> ITER-Center, 1 bld. 3 Kurchatov sq., 123182 Moscow, Russia

<sup>6</sup> National Fusion Research Institute, 169-148 Gwahak-Ro, Yuseong-Gu, Daejeon 305-333, Republic of Korea

<sup>7</sup> Institute of Plasma Physics, Chinese Academy of Science (ASIPP), Hefei, 230031, People's Republic of China

<sup>8</sup> USIPO, Oak Ridge National Laboratory, TN, United States of America

E-mail: [a.nijhuis@utwente.nl](mailto:a.nijhuis@utwente.nl)

Received 1 May 2019, revised 12 June 2019

Accepted for publication 12 July 2019

Published 13 September 2019



CrossMark

## Abstract

The ITER magnet system uses cable-in-conduit conductor (CICC) technology with individual strands twisted in several stages resulting in a rope-type cable, which is inserted into a stainless steel conduit. The combination of high current (up to 68 kA) and background magnetic field (up to 13 T) results in large transverse Lorentz forces exerted on the conductors during magnet system operation. The high transverse forces, accompanied with the cyclic nature of the load, have a strong influence on the conductor properties. The Twente Cryogenic Cable Press is used to simulate the effect of the Lorentz forces on a conductor comparable to the ITER magnet operating conditions. An overview is presented of the AC coupling and hysteresis loss, mechanical deformation characteristics and inter-strand contact resistance measurement results obtained on full-size ITER CICC's measured in the Twente Cryogenic Cable Press. The aim of this work is to characterize conductors' electromagnetic and mechanical properties during cycling of the load up to 30 000 cycles. The evolution of the magnetization (AC coupling loss time constant  $n\tau$ ), mechanical properties and inter-strand resistance  $R_c$  between selected strands is presented along with loading history. The  $R_c$  between first triplet strands is also measured as a function of applied load. It is shown that transverse load cycling has a strong influence on the CICC properties. An overview of the results for eight toroidal field conductors, two central solenoid conductors, three poloidal field conductors of different types (PF1&6, PF4, PF5), one main bus-bar and one correction coil conductor is presented.

Keywords: Nb<sub>3</sub>Sn, NbTi, low  $T_c$  superconductors, CICC, coupling loss, contact resistance, mechanical properties

(Some figures may appear in colour only in the online journal)

## 1. Introduction

ITER relies on a superconducting magnet system to confine and shape the plasma. The magnet system consists from four different types of coils—18 toroidal field (TF), a central solenoid (CS), six poloidal field (PF) and 18 correction coils (CC) [1]. The ITER magnet system uses cable-in-conduit conductor (CICC) technology. The strands in the CICCs are twisted in several stages resulting in a round rope-type cable, which is inserted into a stainless steel conduit. The number of superconducting strands varies from 300 up to 1440 depending on the type of ITER conductor [2]. During magnet operation the combination of high electric current and background magnetic field causes large Lorentz forces (up to  $748 \text{ kN m}^{-1}$  for TF conductors) that results in several effects: a strand bundle and deformation inside the conduit; a gap formation between the conduit and strand bundle [3]; strand motion and hence mechanical heat generation [4]. Strand motion leads to a change in contact resistance between strands and implicitly leads to a change of the coupling currents between strands [5]. The phenomenon of changing resistance was discovered and reported for the first time in 1997 [6]. Furthermore, the electromagnetic load in the ITER magnet system has a cyclic nature thus knowledge of mechanical and electrical properties of conductors as a function of cyclic load is essential to understand and determine the conductor performance over the magnet lifetime.

Although studies on electromagnetic behavior of ITER conductors under relevant electromagnetic conditions performed at the SULTAN facility are known [7–10], the standard test program is limited to about 1000 cycles because a more extensive campaign with a larger number of cycles is considered too time-consuming and costly. Only a few ITER conductor samples were tested in the SULTAN facility up to  $\sim 10\,000$  cycles, while the expected number of load cycles during ITER lifetime is 30 000. The aim of this work is to characterize the mechanical and electromagnetic properties of all types of ITER conductors up to 30 000 load cycles and compare the performance of TF conductors from different suppliers. We use the Twente Cryogenic Cable Press [4, 5, 11] to simulate the expected cyclic Lorentz forces equivalent to the magnet operating conditions.

The results of the press tests are considered being representative for an ITER conductor, however, the monotonous load cycling of 30 000 cycles between zero and peak electromagnetic force will not be exactly representative for the behavior of the ITER coils. First of all, the transverse load on the cables in the press test is a volumetric force while the actual load on the cable in the ITER coils has an electromagnetic nature where the force on the strand layers is accumulated from layer to layer. In addition, the load sequence and applied peak forces during the press test differ from the ITER scenario. The ITER scenario starts with relatively small loads at the first plasma, consequently increasing to larger loads and eventually to peak load at full operation, while during the press test load cycles between zero and peak load are applied. This will lead to different mechanical responses. However, the purpose of this work is to qualify

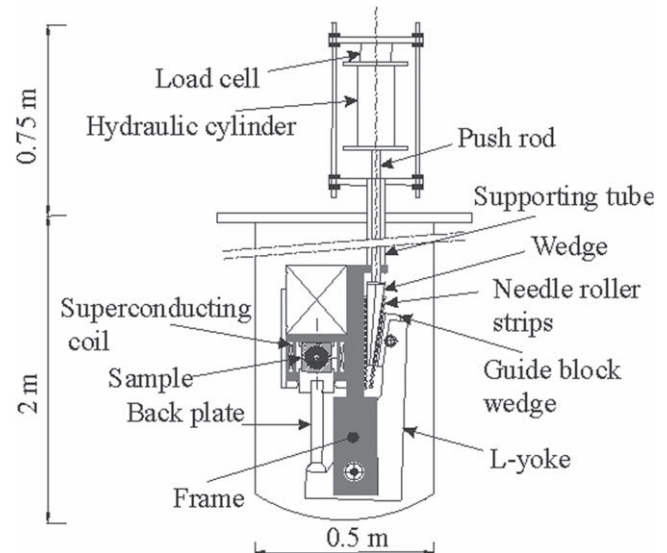


Figure 1. Schematic view of the Twente Cryogenic Cable Press.

ITER conductors and verify their electromagnetic and mechanical response to transverse load with a large number of load cycles.

Here we present an overview of the results for fifteen ITER CICCs from different domestic manufacturers. The evolution of the magnetization (coupling loss time constant  $n\tau$ ) and the inter-strand resistance  $R_c$  between various strands inside the cable along with the loading history is presented as a function of transverse cyclic loading up to 30 000 cycles. In addition, the cable's transverse stiffness and mechanical loss is reported as a function of loading history.

## 2. Experimental setup and sample preparation

### 2.1. Twente Cryogenic Cable Press

The schematic view of the cryogenic press is presented in figure 1. The mechanical part is driven by a hydraulic cylinder at the top of the cryostat generating the force applied to the pushing rod. The pushing rod transmits the force to the cold part of the press through the sealed tube. The press is using a wedge and a lever principle to multiply the force on the sample by 35 times. The force is applied to a conductor section of 400 mm, which is about the length of the last stage twist pitch of ITER conductors. A full twist pitch length is advised for an appropriate AC loss measurement. The influence of sample length and twist pitches on the conductor AC loss have been computed with the code JackPot-AC using various cable lengths up to 10 m, showing negligible difference [12]. On top of this, a detailed comparison between the AC loss evolution of a PF conductor (PFCI) 400 mm short sample in the Twente Press (2005) and the AC loss of the later tested PF Coil Insert (2008) on similar PF conductor (PFCI), but with a length of 50 m showed good agreement [13, 14]. Above mentioned works show that the AC loss measurement done on a 0.4 m sample length is representative for long conductor lengths like in ITER coils.

**Table 1.** Strand combinations for different conductors used for intra-petal resistance measurement according to the corresponding cabling stage.

Cabling stage	CS	PF	TF
First stage	R1–R2, R5–R6	R1–R2, R1–R3, R2–R3	R1–R2, R3–R4
Second stage	R1–R4, R1–R3	R1–R4, R1–R5	R1–R5, R1–R6
Third stage	R1–R5, R1–R6, R1–R7	R1–R6, R1–R7	R1–R3, R1–R7, R3–R7
Fourth stage	R1–R8, R1–R9	R1–R8, R1–R9	R1–R8, R1–R9

The electric part of the press consists of a superconducting dipole magnet and strain gauges attached to the back plate and the L-yoke. The calibrated strain gauges serve to monitor the force applied to the sample. The applied force and conductor's displacement are monitored simultaneously during load–unload cycles that allow determining the conductor's mechanical properties and mechanical losses.

The dipole magnet generates an alternating sinusoidal magnetic field in the sample gap volume for AC loss measurements. A more detailed description of the cryogenic press is given in [15–17]. The press is equipped with 20 current leads and 20 voltage taps that allow for contact resistance measurements. The current leads and voltage taps are connected to the strands specified in tables 1 and 2 for the intra- and inter-petal resistance measurements.

Conductor samples used for the cyclic test in the press setup undergo a preparation procedure described in section 2.2. Since the preparation procedure includes sample handling, hence the sample state cannot be called a virgin state any more. We call the state of a press sample before any load was applied the *initial state*. The inter-strand resistance  $R_c$  and coupling loss measurements are performed first at the initial state of the conductor sample (prior to any load applied) and subsequently at cycle numbers 1, 2, 10, 100, 1000, 10 000, 20 000, and 30 000 in full and zero load states. The full load state means that the load on the sample has reached the peak load as specified in the table 3 for a particular conductor type. The zero load state means that no load is applied to the sample and it is allowed to relax. The maximum sample relaxation is constrained to the initial state defined by the 'limited void fraction' method [5]. During load increase/decrease cycles, the  $R_c$  between strands from the first cabling stage (triplet) are monitored as a function of applied load. All the measurements are made during one cool down session when the press and sample are continuously kept at 4.2 K in a liquid helium bath.

In the case of Lorentz force the load is progressively accumulated over the conductor cross section with a peak load of  $I \times B$ . The real electromagnetic load distribution inside the conductor cannot be simulated in the press that applies homogeneous load. The FEM analysis [18] and analytical calculations show that the average stress inside conductor during real operation is half of the peak Lorentz stress. To stay conservative the peak load applied by the press was selected as 0.75 times  $I \times B$ , which is a bit higher than the average Lorentz stress during magnet operation. The transverse load maxima applied by the press are specified in table 3 for the measured conductors.

**Table 2.** Strand combinations for inter-petal resistance measurement.

Petal #	Contact number
2	R1–R10, R1–R11.
3	R1–R12, R1–R13.
4	R1–R14, R1–R15, R1–R16.
5	R1–R17, R1–R18.
6	R1–R19, R1–R20.

## 2.2. Sample preparation

From every conductor two specimens are prepared, each for an individual conductor sample test. The first specimen, with a length of 400 mm, is tested for the AC loss in a fully virgin condition without further handling and kept in an undivided conduit. This specimen is considered as a reference sample for the AC loss calibration. The AC loss measurements on the virgin sample are done by helium boil off calorimetry combined with the magnetization method by means of a compensated pick-up coil set. This test is performed for comparison and to verify that the conductor handling during press sample preparation did not affect the initial state of the press sample. Or, in other words, to confirm that both samples start with practically similar properties.

The second specimen is used for the cyclic loading test in the cryogenic press. Each sample goes through the standardized preparation procedure before the press test. This procedure is similar for all conductors, except for the heat treatment that is not applied to NbTi type of CICC. The conductors are cut to 400 and 600 mm lengths by spark erosion for the virgin and press sample respectively. Holes with screw thread and bolts are positioned at six locations on both sides of the press sample along the 400 mm of conduit length to secure the initial void fraction, see figure 2(a). The void fraction has a significant influence on the the conductor's coupling loss level and mechanical properties [19, 20]. Thus, it is very important to secure the conductors' void fraction as created during manufacturing. Accordingly, slits are machined along the length by careful milling to separate the conduit into even halves. During machining, only one bolt at the time is removed to allow cutting of the conduit up to a depth where it reaches the cable wrapping but without damaging the strands. This way the void fraction is not changed during the whole preparation process of the press sample. The screw threads are made only in the lower conduit half, then the conduit halves can be pressed to a lower void fraction in the press but the original void fraction cannot exceed the initial state during relaxation of the transverse

**Table 3.** Parameters of measured ITER type conductors.

Parameters	TF	CS	PF1&6	PF2-4	PF5	MB	CC
Sample name	<sup>a</sup>	CS-JAS CS-KAT	PF1&6	PFCN4	PFCN3	MB	CCCN3
Press peak load (kN m <sup>-1</sup> )	578	413	261	202	218	177	32
SC strand type	Nb <sub>3</sub> Sn	Nb <sub>3</sub> Sn	NbTi	NbTi	NbTi	NbTi	NbTi
Strand diameter (mm)	0.82	0.82	0.73	0.73	0.73	0.73	0.73
Strand plating type	Cr	Cr	Ni	Ni	Ni	Ni	Ni
Petal layout	(2sc +1Cu) × 3 × 5 × 5	(2sc +1Cu) × 3 × 4 × 4	3sc × 4 × 4 × 5	[(2sc +1Cu) × 3 × 4 + 1C1] × 5 + 1C2	(3sc × 4 × 4 × 4) +1C3	(2sc +1Cu) × 3 × 5 × (5 + 1C1)	3sc × 4 × 5
Cable layout	Six petals around spiral	Six petals around spiral	Six petals around spiral	Six petals around spiral	Six petals around spiral	Six petals around C3 <sup>b</sup>	Five petals twisted

<sup>a</sup> Eight TF conductors have been tested from different domestic agencies: CMP-RU Russia, OST-EU European Union, HIT-JA Japan, JAS-JA Japan, BEAS-EU European Union, KIS-KO South Korea, WST-CN People's Republic of China, LUV-US USA; two CS conductors from Japanese manufacturers CS-JAS and CS-KAT; three PF conductors of different types (PF1&6, PF4, PF5) one MB and one CC produced by People's Republic of China.

<sup>b</sup> C3 is a bundle of 71 copper strands.



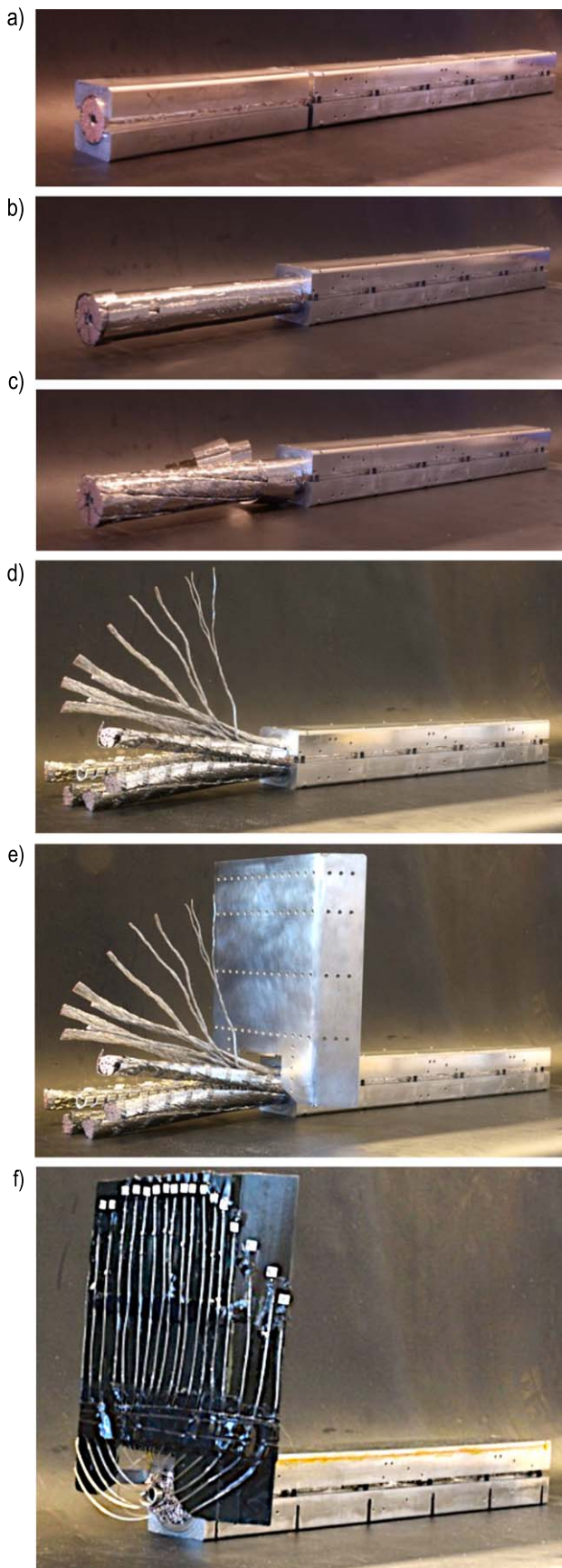


**Figure 2.** Illustration of the conductor press sample preparation steps.

force. The used method allows free compression of the sample while exerting a load but always confines the ultimate relaxation of the cable to that of the initial void fraction. This method is known as ‘limited void fraction’ [5].

Press samples that require contact resistance measurements are cut for that reason to 600 mm length. From one side, along 200 mm of the conductor length, conduit and wraps are completely removed after machining the slits, allowing selection of strands for contact resistance measurements, see figures 2(b)–(d).

Twenty selected strands are mounted on a support plate attached to the conductors’ conduit. Strands not selected for contact resistance measurement are cut close to the conductor conduit, see figure 2(e). After the heat treatment an insulation sheet is placed carefully between strands and support plate and the strands are fixed with Stycast™ epoxy, see figure 2(f).

For the TF and MB samples with circular cross section, a square dummy conduit is used to support and fit the sample in the press gap. The dummy conduit is also used to secure the initial void fraction after cutting the conductor conduit along its length.

The (dummy) conduit is fully prepared for instrumentation (pick-up and compensation coil for magnetization measurement, six displacement meters etc) [15–17]. In the case of a square conduit, the conduit itself is used for the limited void fraction method and instrumentation.

A dummy conduit is also used with the CC conductor sample despite its square shape, to fit the CC sample into the press gap, bridging the small cross-sectional size of the conductor.

Fully prepared Nb<sub>3</sub>Sn conductors are heat treated before measurement according to the heat treatment scheme provided by the manufacturer. The heat treatment takes place in vacuum of at least 10<sup>-5</sup> mbar. A detailed description of the sample preparation procedure for the press test can be found in [5, 20] as well as discussion of the possible influence of handling on conductor properties.

The transverse displacement of the cable is measured by two sets of six displacement meters. The displacement meters are mounted symmetrically distributed along the sample length, two sets of three at each side of the sample.

Figure 3 shows part of the sample with mounted strain gauge-based displacement meter and sketch of the cross section. The displacement meters measure the displacement of the lower part of the conductor (dummy) jacket relative to the upper part. Next to each strain gauge-based displacement meter, a quartz concentric rod in tube gauge is attached, with the rod probing the bottom half of the conduit and the tube probing the upper half. Each rod in tube is connected to a micrometer on the top of the cryostat, probing the difference in displacement, in order to calibrate the strain gauge-based displacement meters. The full load cycle calibration is done during the first load cycle. For every load cycle during the test program, the relative displacement of all six displacement meters is measured. The final conductor displacement,  $d$ , is calculated as the average displacement taken from all six

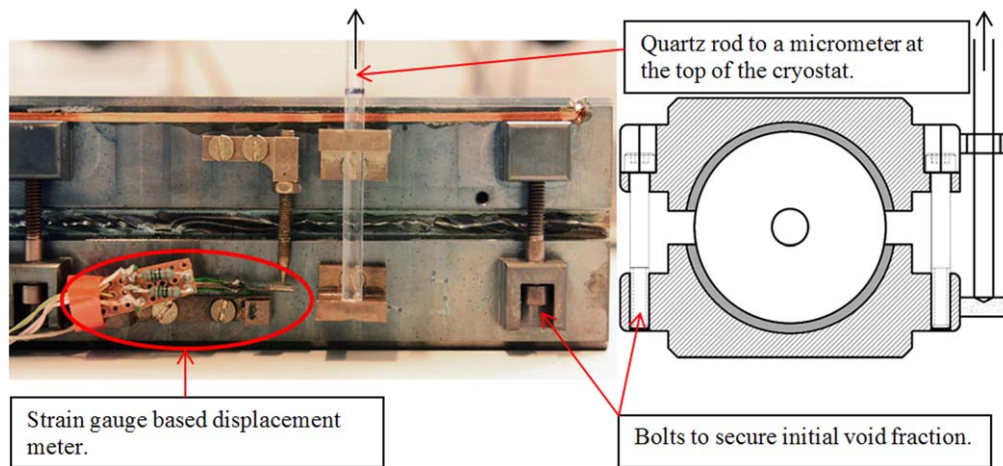


**Figure 3.** Part of the conductor sample with displacement meter and quartz rod attached to the micrometer at the top of the cryostat. Also the bolts that secure the initial void fraction of the cable are shown.

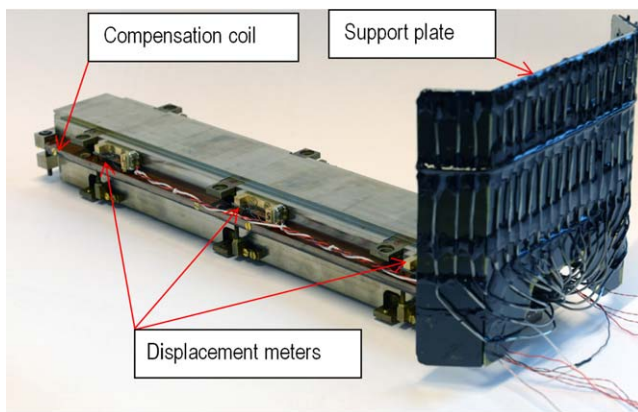


**Figure 4.** Picture of fully prepared sample including pick-up and compensation coils, displacement meters, and strands selected for contact resistance measurements.

displacement meters. The conductor displacement is measured by changing the applied load by small steps and measuring the corresponding displacement after waiting sufficiently long time until the cable relaxation has decayed. Figure 4 shows a sample fully prepared for cyclic load measurement in the cryogenic press.

### 2.3. Instrumentation

The AC losses are measured using the magnetization method by means of a compensated pick-up coil set. The pick-up coil is a saddle type, wound around the upper halve of the sample conduit. The compensation coil is attached to the same halve of the conduit. This assures that the configuration of the coil set remains unchanged during displacement of the lower conduit part with respect to the upper one. Signals from the pick-up and compensation coils are amplified and recorded by the data acquisition system. The applied AC magnetic field is sinusoidal with an amplitude  $B_a$  of  $\pm 0.15$  T and an offset  $B_d$

of 0.35 T. The frequency range of the magnetic field varies from 0.01 to 0.16 Hz. Five magnetization loops  $M(B)$  are recorded and the average value is taken for each magnetic field frequency. The AC loss is given per total volume of superconducting strands. To calculate the superconducting strand volume, the nominal strand diameter was used as specified by the manufacturer for unreacted strands. The volume is calculated as sample length times number of superconducting strands multiplied by the area of one strand cross section.

The conductor displacement given in this paper is the average value over the readings of the six displacement meters.

The contact resistance  $R_c$  between strands is measured by the four-point probe method using 50 A current. A DC background magnetic field  $B_d$  of 0.35 T is applied to exclude the possible influence of a superconducting barrier inside the conductor's strands.

Only superconducting strands are chosen for the contact resistance measurements. The combinations of strands are chosen in a way such that  $R_c$  is measured at least between two strands from each cabling stage inside one petal. The schematic views of strand combinations within one petal (for intra-petal  $R_c$ ) are shown in figure 5 from left to right for CS, PF and TF conductors respectively. The inter-petal contact resistance was measured between strand R1 and at least two randomly chosen strands from each of the other petals. The strand combinations chosen for  $R_c$  measurements are summarized in tables 1 and 2. Table 1 presents the strand combinations for the intra-petal resistance while table 2 presents the strand combinations chosen for the inter-petal resistance measurements. The layout for the inter-petal contact resistance is shown in figure 6 and is the same for all types of conductors.

The contact resistance  $R_c$  of a particular cabling stage is calculated as the average value over strand combinations selected from that stage.



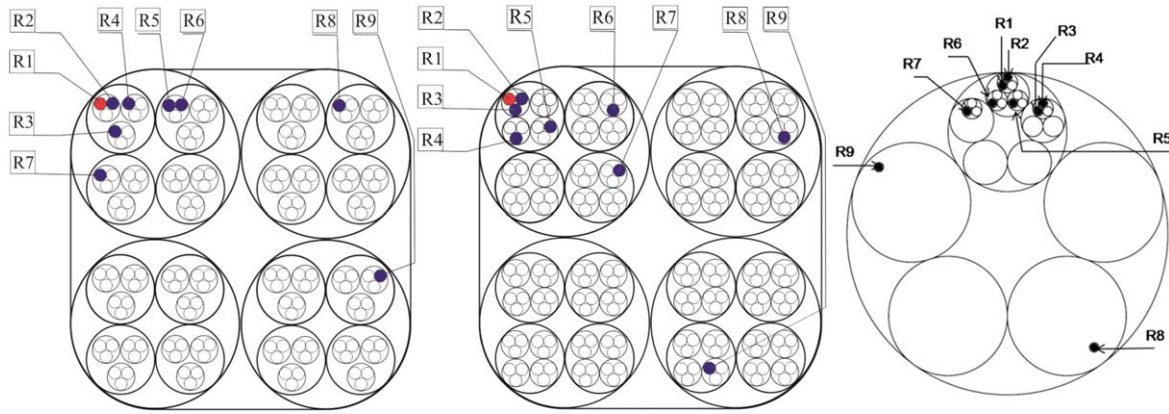


**Figure 5.** Schematic representation of a single petal from left to right for CS, PF, and TF conductors. Rx represents strands selected for contact resistance measurement.

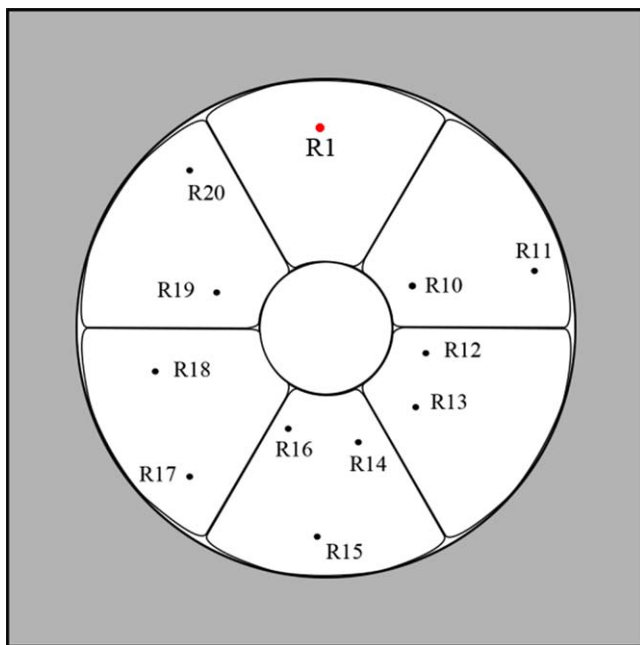


**Figure 6.** Scheme of the strand selection for inter-petal contact resistance measurement. The same layout is used for all types of conductors.

**2.4. Sample specification**

Fifteen samples that cover all types of ITER conductors were measured for qualification in the press. The conductor specification and peak load applied by the press during the tests are listed in table 3.

**3. Experimental results**

The results are summarized in three groups. The first two groups report on data for conductors that utilize Nb<sub>3</sub>Sn strands. The first group presents results for TF conductors only while the second group presents CS conductor results. The third group presents data for NbTi conductors; PF, MB, and CC conductors.

**3.1. AC loss of TF conductors**

Figure 7 shows the loss–frequency dependence of TF conductors at zero load state for the initial state (figure 7(a)) and after 30 000 cycles (figure 7(b)). One can see that the slope of the loss–frequency dependence decreases significantly for all conductors after cycling of the load.

The loss–frequency dependence deviates from linear even at low frequencies of magnetic field. The deviation is especially strong for conductors in the initial state (figure 7(a)) while after load cycling the loss–frequency dependence becomes more linear (figure 7(b)). The loss–frequency dependence is fit by polynomial function of the second order. The second order polynomial function was chosen because linear fitting leads to a significant underestimation of the loss curve slope and hence underestimation of the coupling loss, especially for virgin and initial state conductors. Only data points between 15 and 100 mHz were used to find the slope of the virgin and initial state conductors. From the fit we obtain the loss curve slope  $\alpha$  in the low frequency limit and a constant offset that represents the  $Q_{hys}$  in the conductor.

The initial slope of the loss curve  $\alpha$  is used to calculate the coupling loss time constant  $n\tau$ , with use of relation [21]

$$n\tau = \alpha \frac{\mu_0}{2\pi^2 B_a^2} \quad (\text{ms}), \quad (1)$$

where  $B_a$  is the amplitude of the field ramp and  $\alpha$  is the slope of the loss–frequency dependence curve.

Table 4 presents the  $Q_{hys}$  and  $n\tau$  values measured on fully virgin samples with undivided conduits. The measurements were done by calorimetric method in the dipole magnet with high field quality. The virgin state sample measurement serves as a proof that the conductor handling during press sample preparation does not affect the initial state of the press sample.

Table 5 presents the  $Q_{hys}$  and  $n\tau$  values for the press samples before and after cyclic load test. Though a difference can be observed in  $Q_{hys}$  for zero and full load state of the conductors (figure 8), after 30 000 cycles the distinction



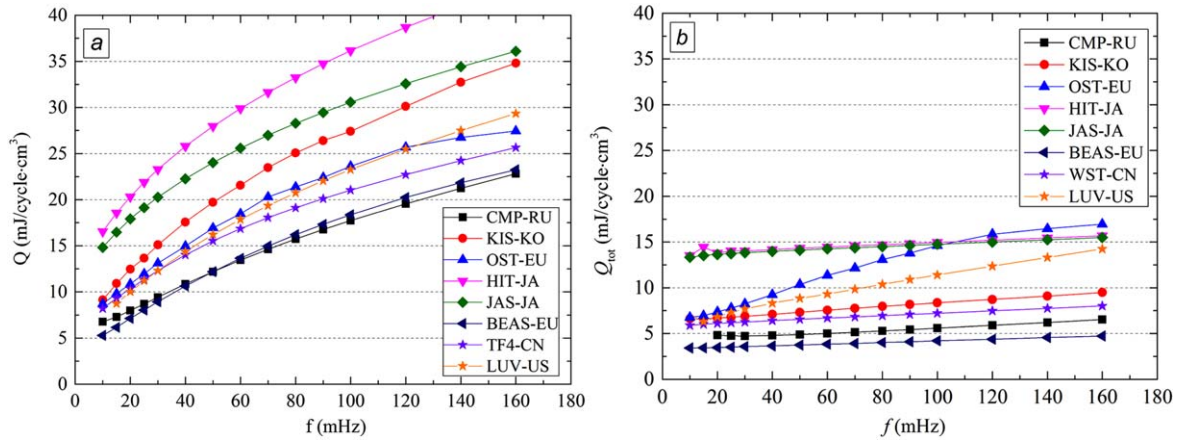


**Figure 7.** AC loss versus frequency of the applied magnetic field for TF conductors in initial state (a) and after 30 000 cycles (b) at zero load.

between both load states is small and within the error bars of the measurement.

Figure 9 shows the evolution of the coupling time loss constant  $n\tau$  as a function of cycle number for TF conductors at zero and full load. Though the initial  $n\tau$  values vary from  $446 \pm 10$  ms for the CMP-RU sample to  $994 \pm 35$  ms for the HIT-JA sample, the general evolution trend is the same for all TF conductors. The largest decrease of the coupling loss is observed between the initial state and after the first cycle for all TF conductors. After the second cycle the subsequent change in coupling loss already becomes smaller. The  $n\tau$  decreases fast within the first ten loading cycles. After cycle 100, all samples show saturation in the evolution of  $n\tau$  with cycling except the LUV-US sample. The LUV-US sample shows a very gradual decrease of the  $n\tau$  saturating at the relatively high level of 165 ms at zero load while the rest of the samples saturates at  $\sim 46 \pm 20$  ms after 30 000 cycles. Under full load the saturation level of  $n\tau$  values is higher compared with the zero load state. Most conductors show a saturation level of  $\sim 105 \pm 20$  ms under full load, while two conductors deviate; KIS-KO and LUV-US. The KIS-KO conductor reaches its saturation at a level of  $\sim 189$  ms while the  $n\tau$  value of LUV-US conductor saturates at the level of  $\sim 267$  ms at full load.

The rather high  $n\tau$  of the OST-EU sample can be explained by tin leakage that occurred during the sample heat treatment (see section 4). Though we implement the correction with reference to the initial state  $n\tau$  value, the correction factor might vary from cycle to cycle due to the different contact pattern between strands. That makes it impossible to determine the  $n\tau$  values with high certainty for the OST-EU sample.

### 3.2. Mechanical properties of TF conductors

Figure 10 shows a typical characteristic of the displacement versus applied load of TF conductors at different load cycles. The BEAS-EU conductor is used as an example. The curves show the typical visco-elasto-plastic deformation as was

observed earlier on CICC with clear hysteresis behavior during load–unload cycling [4].

The largest displacement during a full cycle is always observed at the first cycle together with the largest hysteresis loop. The area of hysteresis loops decreases successively with the cycle number as illustrated in figure 10. Figure 11 shows the absolute deformation of TF conductors at maximum load as a function of the cycle number.

The load–displacement behavior with cycles changes since most of the plastic deformation occurs at the first load cycle. As the number of loading cycles increases, the part of plastic deformation reduces and after ten cycles, the conductor exhibits mainly elastic behavior. However, figure 11 illustrates that a relatively small component of plastic deformation remains with increasing number of cycles, suggesting continued strand deformation with load cycling.

All measured TF conductors display similar evolution of the displacement at maximum load versus cycle number. At the first cycle, the conductor compaction is in the range between  $941 \mu\text{m}$  for LUV-US (the lowest displacement) and  $1242 \mu\text{m}$  for the BEAS-EU conductor (the highest displacement). The conductors' absolute deformation increases further with cycling of the load. Compared with the first cycle, all TF conductors show a similar increase in the maximum displacement of  $360 \pm 60 \mu\text{m}$  after 30 000 loading cycles. An increase in the displacement rate was clearly observed for practically all TF conductors (except WST-CN and LUV-US samples) between cycles 10 000 and 30 000, see figure 11.

The area enclosed by a hysteretic displacement loop as shown in figure 10, represents the mechanical loss  $Q_m$  during cycling of the load. The mechanical loss is the amount of heat generated in the conductor during one full cycle due to strand friction and deformation. The mechanical loss dissipated during one full cycle is calculated as

$$Q_m = \oint F_y \cdot dy \quad (\text{J/cycle}), \quad (2)$$

where  $F_y$  is the applied transverse force and  $dy$  is the conductor transverse deformation.

Figure 12 shows the mechanical loss evolution with the number of load cycles of all measured TF conductors. The

**Table 4.** AC coupling loss time constants and hysteresis loss values for virgin TF conductors.

	Applied field T	CMP-RU	KIS-KO	OST-EU	JAS-JA	HIT-JA	BEAS-EU	WST-CN	LUV-US
$Q_{hys}$ (mJ/cycle cm <sup>3</sup> ) virgin sample	±0.15 T	11.5 ± 0.1	9.3 ± 0.2	6.3 ± 0.2	10.7 ± 0.4	14.2 ± 0.2	5.0 ± 0.2	7.4 ± 0.3	6.8 ± 0.3
	0.2–0.5 T	4.7 ± 0.1	6.9 ± 0.2	6.3 ± 0.2	12.6 ± 0.2	13.4 ± 0.2	3.5 ± 0.2	7.0 ± 0.2	5.8 ± 0.1
$n\tau$ (ms) virgin sample	±0.15 T	380 ± 10	779 ± 14	687 ± 23	666 ± 60	834 ± 30	547 ± 11	552 ± 25	642 ± 10
	0.2–0.5 T	510 ± 10	825 ± 14	608 ± 17	801 ± 60	1005 ± 30	551 ± 17	529 ± 14	668 ± 5

**Table 5.** Measured values for AC loss, mechanical deformation and stiffness of TF conductors.

Strands route		CMP-RU	KIS-KO	OST-EU	JAS-JA	HIT-JA	BEAS-EU	WST-CN	LUV-US
		Bronze	Tin	Tin	Bronze	Bronze	Bronze	Tin	Tin
$Q_{hys}$ (mJ/cycle cm <sup>3</sup> )	Initial state	4.7 ± 0.1	6.4 ± 0.2	6.6 ± 0.2	13.1 ± 0.2	13.6 ± 0.2	3.5 ± 0.2	6.7 ± 0.2	5.8 ± 0.2
	Final cycle	4.6 ± 0.1	6.2 ± 0.1	5.8 ± 0.3	13.4 ± 0.2	13.7 ± 0.2	3.3 ± 0.1	5.8 ± 0.1	5.6 ± 0.2
$n\tau$ (ms) initial state		446 ± 10	919 ± 50	605 ± 6 <sup>a</sup>	802 ± 25	994 ± 35	584 ± 6	641 ± 16	736 ± 15
$n\tau$ (ms) final cycle	Zero load	36 ± 10	62 ± 4	189 ± 14 <sup>a</sup>	46 ± 11	46 ± 10	24 ± 2	48 ± 1	227 ± 3
	Full load	89 ± 10	189 ± 4	274 ± 14 <sup>a</sup>	106 ± 3	126 ± 10	94 ± 3	111 ± 1	267 ± 4
$Q_m$ (mJ/cycle cm <sup>3</sup> )	First cycle	334	350	305	380	340	416	327	264
	Final cycle	26	21	20	23	10	19	19	16
Maximum displacement ( $\mu$ m)		1370	1435	1473	1603	1426	1631	1433	1243
$E_y$ (GPa)	First cycle	2.1	2.1	2.2	1.9	2.1	2.0	2.2	2.1
	Final cycle	1.6	1.6	1.7	1.4	1.5	1.5	1.6	1.6

<sup>a</sup>  $n\tau$  values are given after correction.

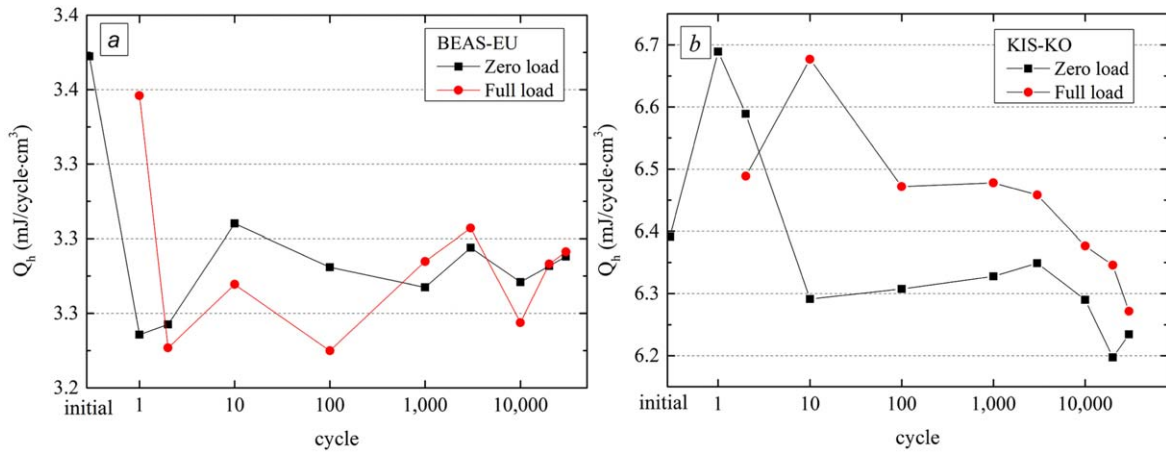


Figure 8. Hysteresis loss values of BEAS-EU (left) and KIS-KO (right) samples as a function of load cycle number.

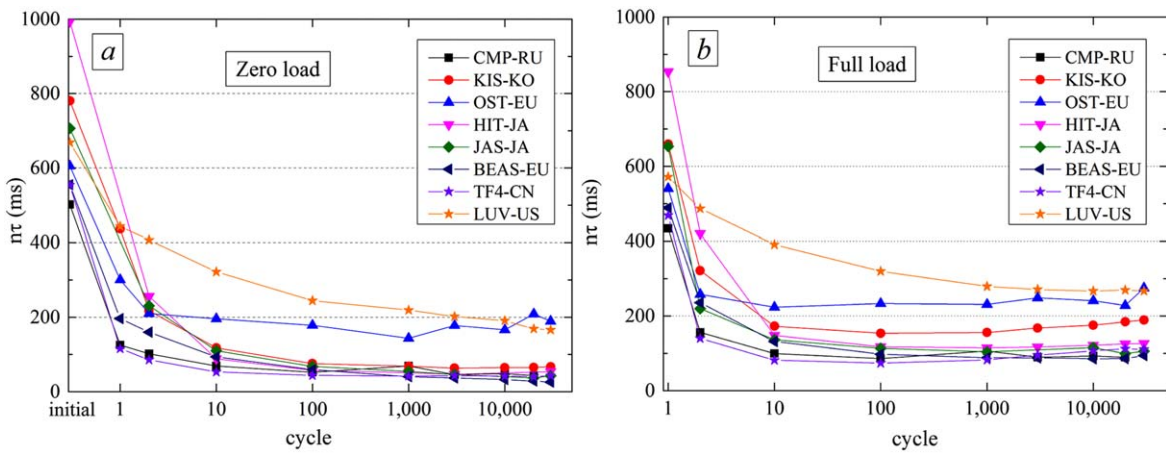


Figure 9. Evolution of the coupling loss time constant  $n\tau$  with the number of load cycles for unloaded (left) and fully loaded (right) state of TF conductors.

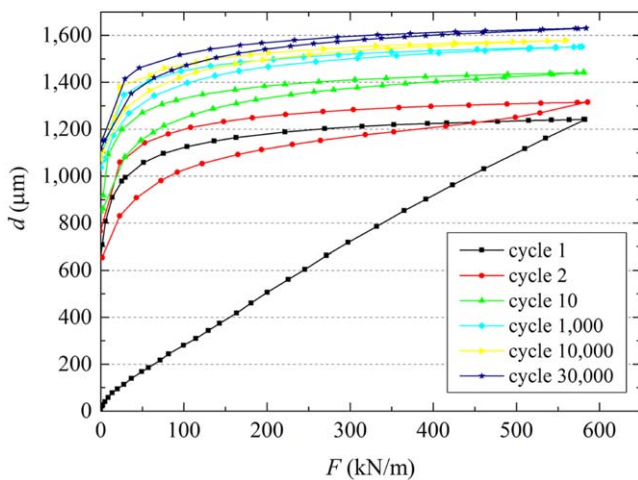


Figure 10. Example of typical force–displacement curves for different number of cycles of the BEAS-EU sample.

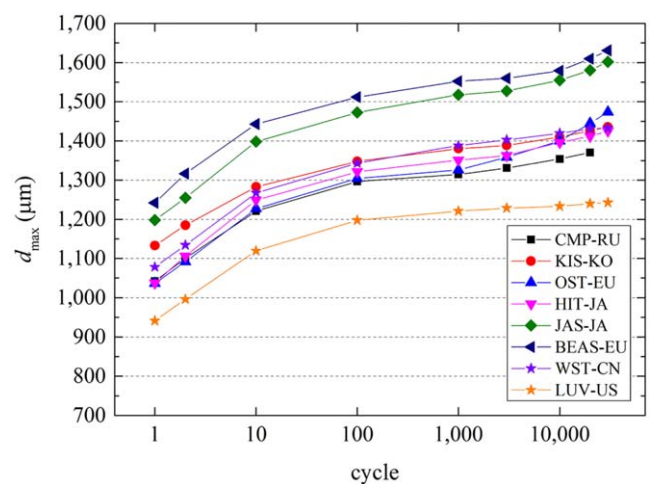
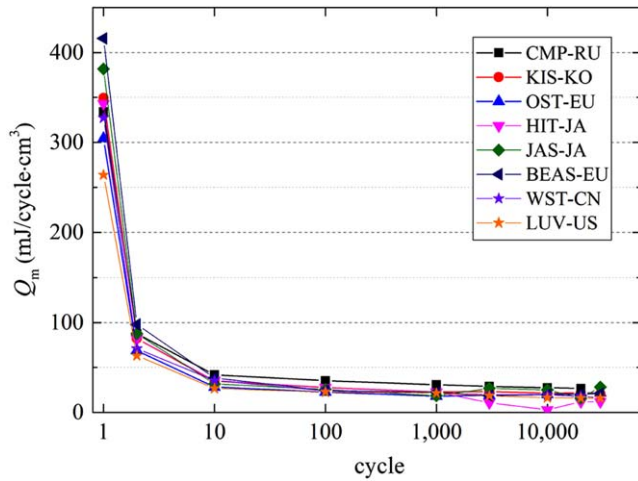
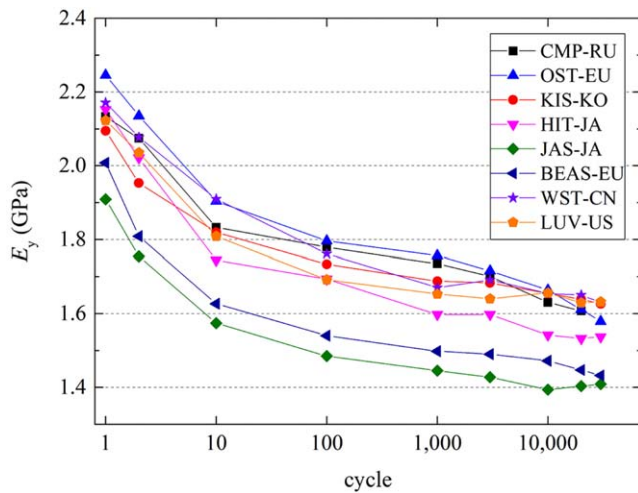


Figure 11. Evolution of TF conductors’ displacements at maximum applied load versus cycle number.





**Figure 12.** Evolution of the mechanical loss with number of load cycles for all TF conductors.



**Figure 13.** Evolution of the elastic modulus at maximum applied load as a function of cycle number for all TF conductors.

mechanical loss is normalized per total strand volume in the sample. All measured TF conductors show very similar behavior of mechanical loss versus the number of load cycles. At the first cycle, the mechanical loss of TF conductors varies from 263 mJ/cycle cm<sup>3</sup> for the LUV-US conductor to 416 mJ/cycle cm<sup>3</sup> for BEAS-EU. Already at the second cycle the mechanical loss becomes lower than 100 mJ/cycle cm<sup>3</sup> for all conductors. After 100 cycles the mechanical loss for the measured TF conductors saturate at the level of 31 ± 4 mJ/cycle cm<sup>3</sup>.

In this work, the term *E*-modulus of the conductors in transverse direction is used as the ratio of force and displacement. The effective elastic modulus of a conductor in transverse direction is defined in [4] as

$$E_y = \frac{D \cdot F_y}{A_y \cdot d_y} \quad (\text{Pa}), \quad (3)$$

where *D* is the conductor diameter, *A<sub>y</sub>* (m<sup>2</sup>) is the average longitudinal cables cross section (projected cable area) and *d<sub>y</sub>*,

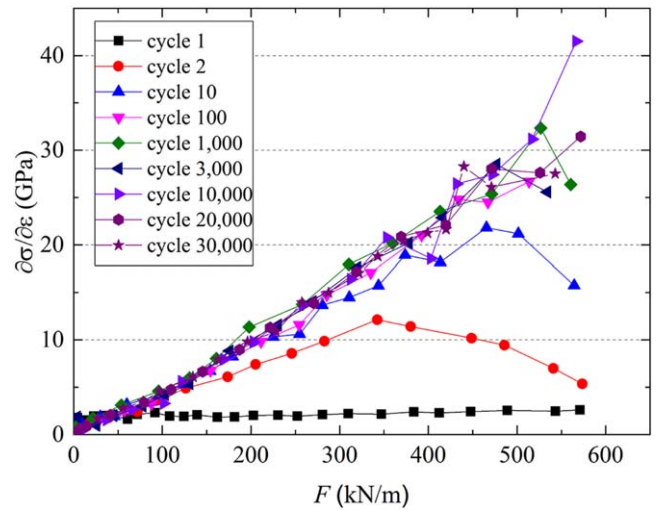


**Figure 14.** Evolution of the dynamic elastic modulus versus applied load for different cycle numbers of the BEAS conductor upon increasing load.

is the absolute conductor deformation relative to its initial contour. The displacement values under full load are taken to calculate the elastic moduli. These displacements are relative to the initial sample state and so the values include the displacement at zero load.

The evolution of *E<sub>y</sub>* at maximum applied load as a function of cycle number is shown in figure 13. All conductors exhibit a similar evolution of *E<sub>y</sub>*. Among the measured TF conductors, the JAS-JA and BEAS-EU conductors are the softest.

The term ‘dynamic modulus’ refers to changes in the quasi-static load–displacement measurement results. This represents the conductor stiffness at a certain level of stress and strain and is described as

$$\frac{\partial \sigma_y}{\partial \varepsilon_y} = \frac{D}{A} \frac{\partial F_y}{\partial d_y} \quad (\text{Pa}), \quad (4)$$

where *σ<sub>y</sub>* is the transverse stress and *ε<sub>y</sub>* the transverse strain. The dynamic *E*-modulus is a characteristic representing the change of the stiffness with increasing load. It shows the influence of the cable twist pattern on the cable deformation characteristics, besides the transverse stiffness and deformation properties of the Nb<sub>3</sub>Sn and softer copper strands. At low loads, a small value of the dynamic *E*-modulus represents a marginal impact of contact stress between crossing strands and the main deformation of strands in the cable is due to bending. The higher the force becomes, the closer the dynamic *E*-modulus approaches the strand transverse contact stiffness [22]. The larger the number of cycles at full cable load, the larger the strand deformation due to contact stress (pinching) becomes [22]. This is reflected by the continuous increase of deflection in figure 11.

Figure 14 shows the typical evolution of the dynamic elastic modulus for TF conductors (BEAS TF conductor). During the first loading, the ∂*σ<sub>y</sub>*/∂*ε<sub>y</sub>* remains around 2 GPa. That shows that most of the strand bending deformation and displacement take place at the first load. After 100 cycles, the

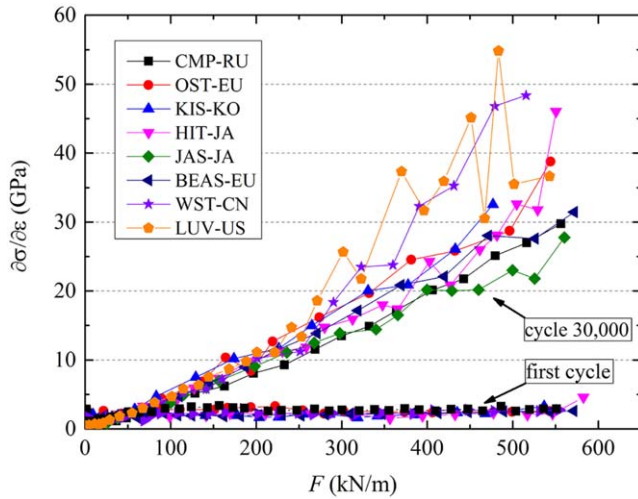


**Figure 15.** Dynamic elastic modulus of all TF conductors versus applied load for the first cycle and the last cycle upon increasing load.

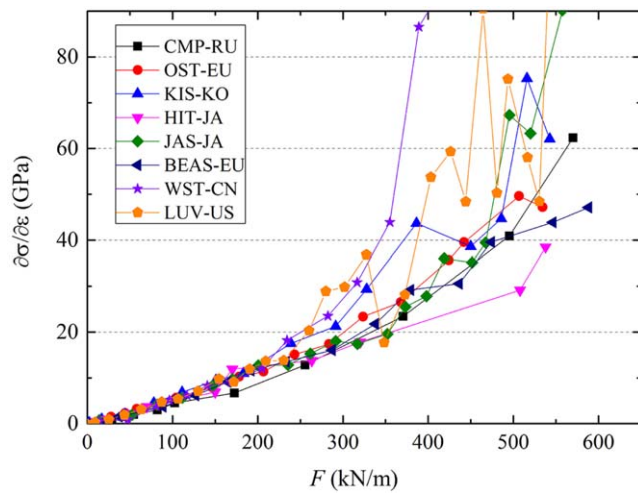


**Figure 16.** Dynamic elastic modulus of TF conductors versus applied load for the last cycle upon releasing the load, cycle 30 000.

$\partial\sigma_y/\partial\varepsilon_y$  seems stabilized and keeps following the same trajectory for subsequent cycles.

Figure 15 shows the comparison of  $\partial\sigma_y/\partial\varepsilon_y$  for all measured TF conductors as a function of applied load for the first and the last loading cycle. At the first cycle upon increasing load, the  $\partial\sigma_y/\partial\varepsilon_y$  stays at the level of  $\sim 2$  GPa for all TF conductors. The evolution of  $\partial\sigma_y/\partial\varepsilon_y$  between the first cycle and cycle 100 is specific for each conductor. However, from cycle 100,  $\partial\sigma_y/\partial\varepsilon_y$  follows a trajectory that is about the same for all conductors as illustrated in figure 15. The final value of  $\partial\sigma_y/\partial\varepsilon_y$  at cycle 30 000 at full load of  $578 \text{ kN m}^{-1}$ , approaches a level of  $\sim 30$  GPa for all TF conductors. Only WST-CN and LUV-US conductors show a systematically higher  $\partial\sigma_y/\partial\varepsilon_y$  value reaching  $\sim 50$  GPa at full load. Despite the different overall compression, the final stiffness is similar for most of the TF conductors and only WST-CN and LUV-US conductors exhibit a somewhat higher stiffness.

The magnitude of the dynamic elastic modulus is different for the load and unload parts of the cycle since the

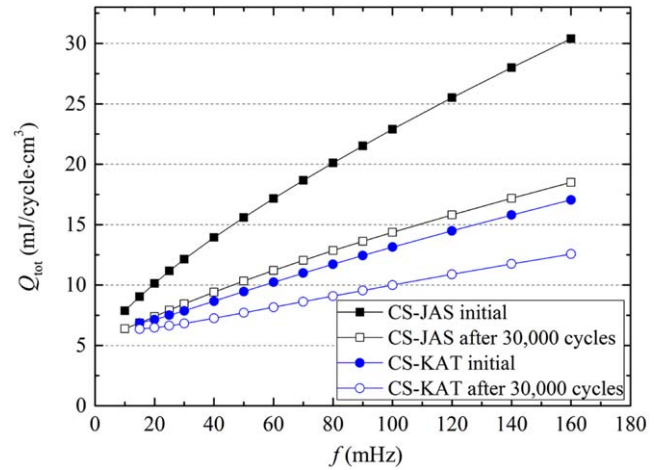


**Figure 17.** AC loss versus the magnetic field frequency for CS type conductors in initial state (solid symbols) and after 30 000 loading cycles at zero load (open symbols).

displacement follows a different route during increase and decrease of the load, showing clear hysteretic behavior during load cycling as depicted in figure 10. The dynamic elastic modulus upon releasing the load follows the same trajectory as observed during the first cycle figure 16 while the trajectory itself is unique for each sample.

Upon releasing the load, the  $\partial\sigma_y/\partial\varepsilon_y$  decreases from  $\sim 55$  GPa at full load to zero GPa in fully unloaded state. The WST-CN and LUV-US conductors again show a higher  $\partial\sigma_y/\partial\varepsilon_y$  value compared with the rest of the TF conductors; during release of the load the  $\partial\sigma_y/\partial\varepsilon_y$  of WST-CN and LUV-US samples decreases from  $\sim 100$  GPa at full load to zero GPa in fully unloaded state.

### 3.3. AC loss of CS conductors

Two CS conductors were measured in the cryogenic press with cyclic loading. The first sample is CS-JAS relying on Jastec  $\text{Nb}_3\text{Sn}$  bronze processed strands. The second sample is CS-KAT made of KAT strands based on the internal tin route [23]. Similar to TF conductors, virgin state samples with undivided conduits were also measured for AC loss in the AC dipole magnet by calorimetric method. Table 6 presents  $n\tau$  and  $Q_{hys}$  values for the virgin state CS conductors.

The peak load applied to the CS conductors is  $413 \text{ kN m}^{-1}$ , which is lower than that applied to TF conductors. Figure 17 shows the loss–frequency dependence of the CS-JAS and CS-KAT conductors at the initial and final state after 30 000 cycles in the press. Similar to TF conductors, the initial slope  $\alpha$  and  $Q_{hys}$  values for each cycle were obtained.  $Q_{hys}$  values of CS conductors in the initial state and after 30 000 load cycles are presented in table 7 for zero applied load. Figure 18 shows the evolution of the  $Q_{hys}$  for the CS conductors with the number of loading cycles. Both samples show a decrease in hysteresis loss with load cycling. The decrease is especially pronounced in the zero load state.

Figure 19 shows the evolution of the coupling loss time constant for both CS conductors at zero and full load states. The initial  $n\tau$  value is 562 ms for the CS-JAS and 242 ms for

**Table 6.** AC loss parameters of the virgin state CS conductors.

Sample	$Q_{hys}(\text{mJ}/\text{cycle cm}^3)$		$n\tau$ (ms)	
	$B_a = \pm 0.15 \text{ T}$	$B_a = 0.2\text{--}0.3 \text{ T}$	$B_a = \pm 0.15 \text{ T}$	$B_a = 0.2\text{--}0.3 \text{ T}$
CS-JAS	$22 \pm 0.2$	$6.6 \pm 0.2$	$577 \pm 20$	$549 \pm 14$
CS-KAT	$6.3 \pm 0.1$	$5.5 \pm 0.2$	$263 \pm 6$	$242 \pm 3$

the CS-KAT conductor. The initial  $n\tau$  of CS-JAS is comparable with the initial values of TF conductors while CS-KAT sample has much lower initial  $n\tau$  value.

No  $n\tau$  saturation was found with cycling for the CS-JAS conductor, even after 30 000 load cycles. The  $n\tau$  value remains at the quite high level of 363 ms at full load and 297 ms at zero load. The CS-KAT sample showed different behavior with initially a low  $n\tau$  value saturating after 1000 cycles at the level of 179 ms at full load and 144 ms at zero load.

### 3.4. Mechanical properties of CS conductors

The CS-JAS conductor reached a displacement of  $554 \mu\text{m}$  at maximum applied load during the first load. The CS-KAT conductor reached a displacement of only  $349 \mu\text{m}$  at maximum load at the first cycle, see figure 20.

The displacement of the CS-JAS sample has a linear behavior with cycle number without any sign of saturation even up to 30 000 cycles as illustrated in figure 20. The total compaction of the CS-JAS conductor at the final cycle is  $593 \mu\text{m}$ , that gives only  $39 \mu\text{m}$  change between cycles 1 and 30 000 (the  $\Delta d_{\text{max}}$  for TF conductors is about ten times higher). At the same time the displacement of the CS-KAT sample saturates after 10 000 cycles at a level of  $450 \mu\text{m}$ , which gives  $100 \mu\text{m}$  sample compaction between cycles 1 and 30 000.

The mechanical loss of the CS conductors for a full cycle versus the load cycle number is shown in figure 21. For the first cycle, the mechanical loss is  $206 \text{ mJ}/\text{cycle cm}^3$  for the CS-JAS and  $132 \text{ mJ}/\text{cycle cm}^3$  for the CS-KAT conductor. The mechanical loss decreases quickly between the first and second cycles and saturates after ten cycles at the level of  $\sim 13 \text{ mJ}/\text{cycle cm}^3$  for both CS conductors, which is about twice as low compared to the saturation level of TF conductors.

Using formula (4) we calculated effective elastic modulus of the CS conductors at selected cycles. The evolution of the effective elastic modulus versus loading cycle number for the CS conductors is shown in figure 22. During the first cycle the effective elastic modulus of the CS-JAS conductor reaches 3.2 GPa at the maximum load. The CS-KAT sample has an effective elastic modulus of 4.8 GPa at first full load. The CS conductors are much stiffer than the TF conductors that have an elastic modulus at first cycle in the range of 1.9–2.2 GPa. During cycling of the load, the effective elastic modulus of the CS-JAS conductor exhibits a rather gradual decrease with cycle number reaching 2.9 GPa after 30 000 cycles. Cycling of the load has a larger effect on the effective elastic modulus of the CS-KAT conductor. During the first 100 cycles, the  $E_y$

of CS-KAT decreases from 4.8 to 3.7 GPa and stays at that level till the end of cycling.

Similar to TF conductors, the dynamic elastic modulus  $\partial\sigma_y/\partial\varepsilon_y$  for CS samples was calculated using of formula (5). Figure 23 shows the dynamic elastic moduli of the CS conductors upon increasing load. During the first load, the  $\partial\sigma_y/\partial\varepsilon_y$  remains around 3 GPa for the CS-JAS conductor, the CS-KAT conductor with stiffer internal tin type of strands has a  $\partial\sigma_y/\partial\varepsilon_y$  of around 5 GPa at first cycle. Both CS conductors show the same values of dynamic elastic modulus already at cycle 10 upon increasing load as illustrated in figure 23. Similar behavior of  $\partial\sigma_y/\partial\varepsilon_y$  means that both CS conductors have the same stiffness after cycle 10 despite of the different type of strands used. At the final cycle, the  $\partial\sigma_y/\partial\varepsilon_y$  values are the same for the CS-JAS and CS-KAT conductors, approaching a level of  $\sim 25 \text{ GPa}$  at full load of  $413 \text{ kN m}^{-1}$ . The magnitude of the dynamic elastic moduli are different for loading and unloading parts of the cycle due to hysteretic behavior of the displacement during cycling of the load. Figure 24 illustrates the behavior of the  $\partial\sigma_y/\partial\varepsilon_y$  upon unloading of the CS conductors. The dynamic elastic modulus follows the same trajectory for both conductors already from the first cycle decreasing from  $\sim 40 \text{ GPa}$  at full load to 0 GPa at zero load for all cycles as shown in figure 24. A summary of CS conductor parameters measured in initial condition and after 30 000 load cycle is given in table 7.

### 3.5. AC loss of NbTi CCICs

PF, main bus-bar (MB) and CC type of conductors, from which three different types of PF conductors were measured, represent the ITER NbTi conductors. The sample named PFCN3 is a PF5 type conductor, the sample named PFCN4 is a PF2-4 type of conductor and sample PF1&6 is a PF1&6 type of conductor.

Similar to  $\text{Nb}_3\text{Sn}$  conductors, the AC loss of the virgin samples was measured in the AC dipole setup by calorimetry. The results of virgin conductor's AC loss in the dipole setup are presented in the table 8.

Figure 25 shows the loss–frequency dependencies for the NbTi conductors measured in the press in the initial state prior to any load applied (figure 25(a)) and after 30 000 loading cycles (figure 25(b), fully unloaded state). The initial slope of the loss–frequency dependence of the NbTi conductors is increased after load cycling contrary to the decrease observed earlier for the  $\text{Nb}_3\text{Sn}$  type conductors (figures 7, 17). The loss–frequency dependency of the NbTi conductors was fit with a linear function to obtain the loss curve initial slope  $\alpha$  and constant offset that represents the hysteresis loss  $Q_{hys}$ .

**Table 7.** Measured parameters of the CS conductors.

Sample	$Q_{hys}$ (mJ/cycle cm <sup>3</sup> )		$n\tau$ (ms)			$Q_m$ (mJ/cycle cm <sup>3</sup> )		Final displacement ( $\mu$ m)	$E_y$ (GPa)	
	Initial state	Final cycle	Initial state	Final cycle zero load	Final cycle full load	First cycle	Final cycle		First cycle	Final cycle
CS-JAS	5.7 $\pm$ 0.1	5.2 $\pm$ 0.1	561 $\pm$ 11	298 $\pm$ 4	363 $\pm$ 5	205	132	593	3.2	2.9
CS-KAT	5.2 $\pm$ 0.1	4.9 $\pm$ 0.1	242 $\pm$ 6	144 $\pm$ 2	179 $\pm$ 2	12	13	450	4.8	3.6



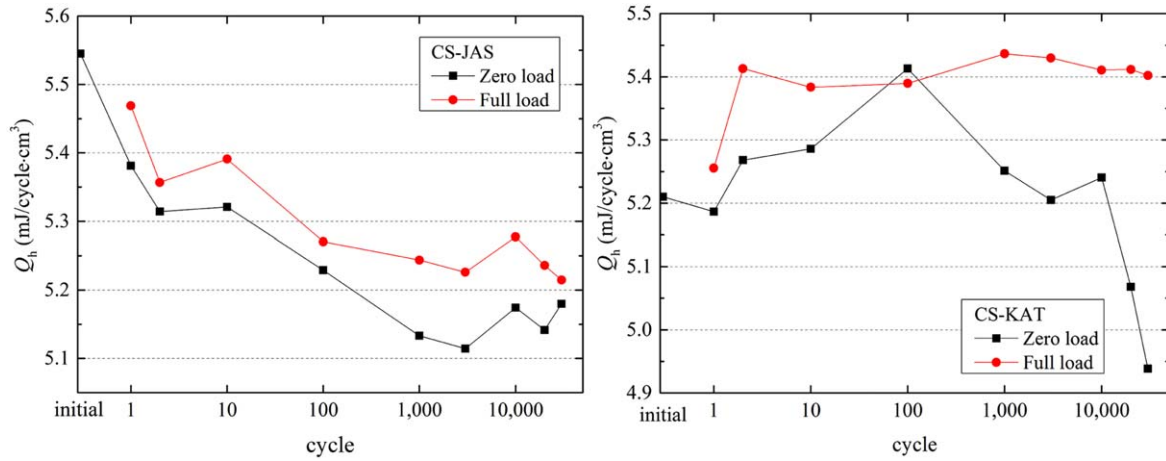


Figure 18. Hysteresis loss evolution for CS-JAS and CS-KAT samples with cycle number.

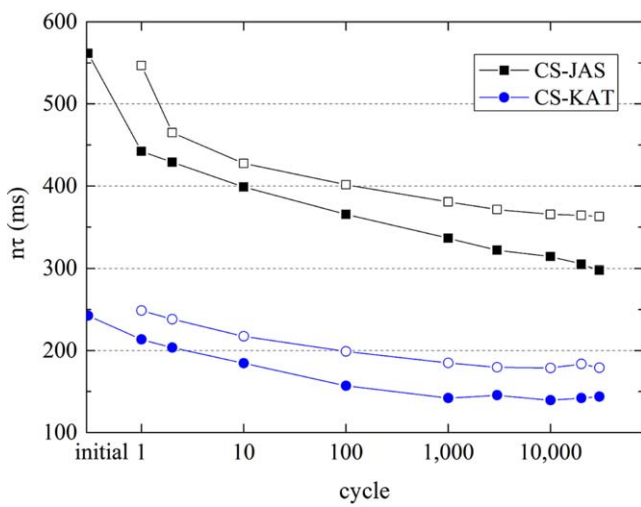


Figure 19. Evolution of  $n\tau$  values with cycle number for the CS conductors, solid symbols represent zero load, open symbols full load.

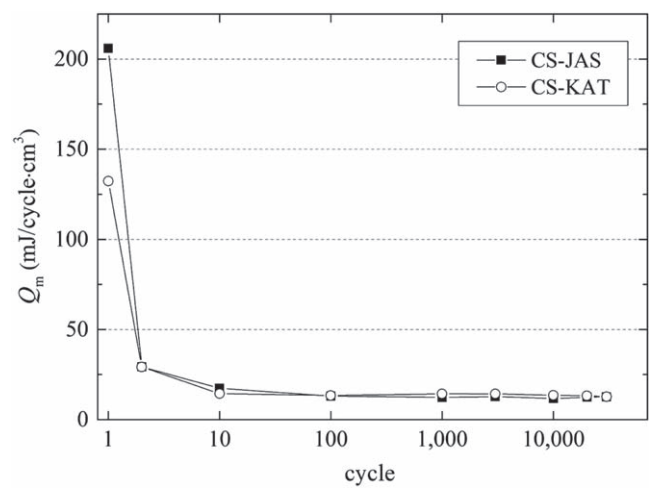


Figure 21. Evolution of the mechanical loss with load cycle number for the CS conductors.

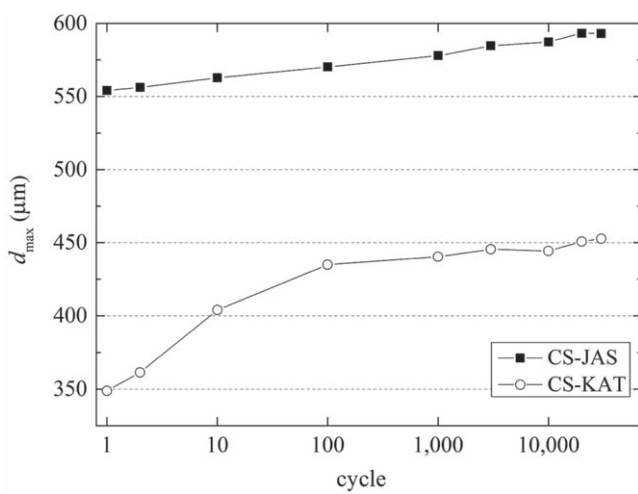


Figure 20. Evolution of the displacement at the maximum applied load with load cycle number for the CS conductors.

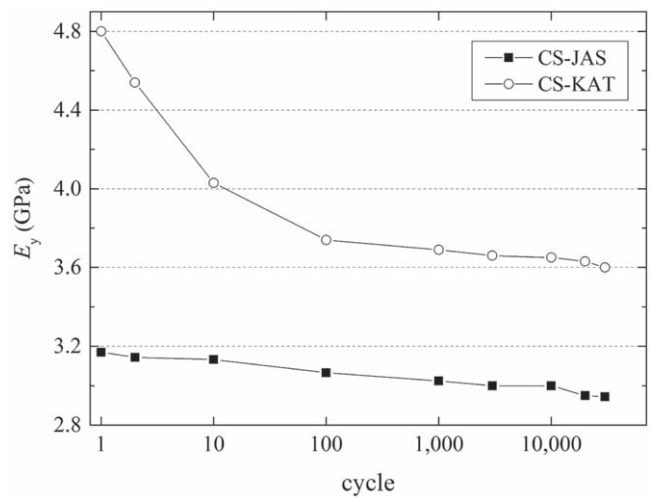
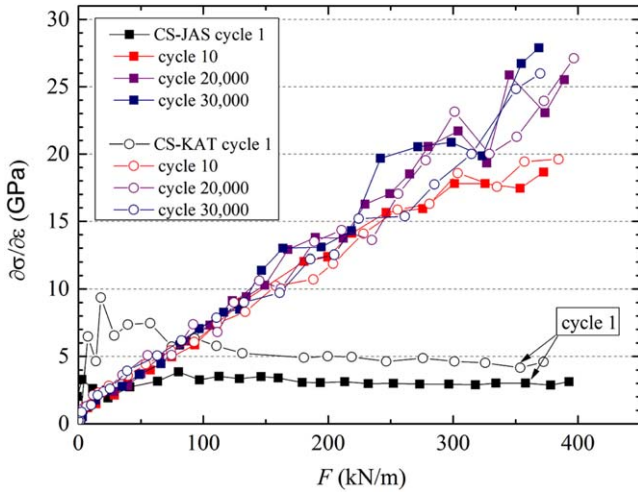
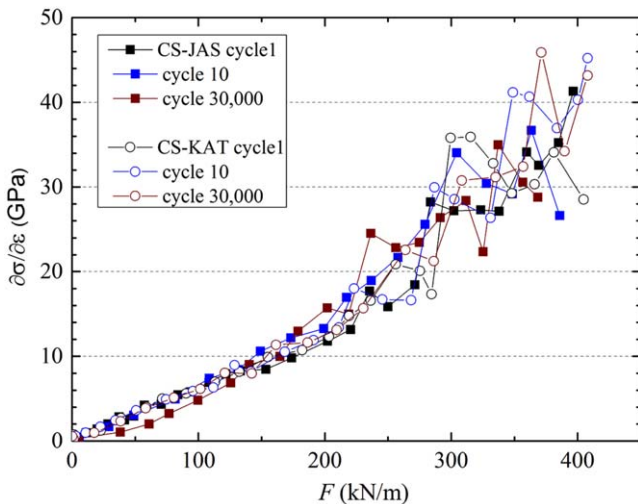


Figure 22. Evolution of the effective elastic moduli with load cycle number for the CS conductors.



**Figure 23.** Evolution of the dynamic elastic modulus of the CS conductors versus applied load for cycles 1, 10, 20 000 and 30 000 upon increasing load. The CS-JAS sample is represented by filled marks while the CS-KAT sample is represented by open marks.



**Figure 24.** Evolution of the dynamic elastic modulus versus applied load for different cycle numbers upon unloading for the CS conductors.

The  $Q_{hys}$  values for NbTi conductors at zero load are given in table 9 before and after cycling of the load.

Similar to Nb<sub>3</sub>Sn conductors by using formula (2), the coupling loss time constant  $n\tau$  for the NbTi conductors was calculated. Figure 26 shows the evolution of the time constant  $n\tau$  with load cycles for zero load (figure 26(a)) and full load conditions (figure 26(b)).

### 3.6. Mechanical properties of NbTi CCIC

The limits of the maximum transverse load for the NbTi conductors are specified in table 3. The PF, CC, and MB conductors are subjected to lower loads in the ITER coils than TF and CS conductors. A typical displacement versus applied load for an NbTi conductor is presented in figure 27. The PFCN3 sample was chosen as an example. The displacement

curves show the hysteresis behavior during load–unload cycles.

Figure 28 presents deformation of the NbTi conductors at the maximum applied load versus cycle number. The largest displacement is observed for the PFCN3 and MB samples. The CCCN3 sample has the smallest displacement, which is mainly associated with the lowest peak load of  $32 \text{ kN m}^{-1}$ . The displacement of the PF1&6 and CCCN3 samples is almost constant at the maximum load during load cycling while the PFCN3, PFCN4 and MB samples show an increase in displacement under full load during the first 100 cycles and saturate after cycle 1000. Note that all measured NbTi conductors have different limits of maximum load.

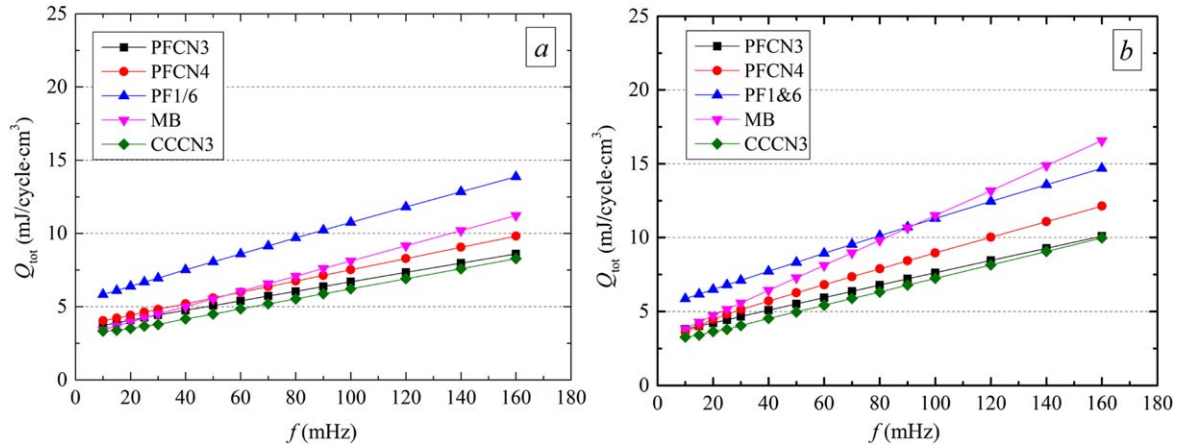
Figure 29 presents the mechanical loss of the NbTi conductors versus cycle number. The loss at the first cycle varies from  $3 \text{ mJ cm}^{-3}$  for the CCCN3 sample to  $60 \text{ mJ cm}^{-3}$  for the PFCN3 sample.

Figure 30 presents the effective elastic modulus  $E_y$  of the NbTi conductors in transverse direction as a function of cycle number. The effective elastic moduli of all samples except PF1&6 decrease slightly within the first 100 cycles and remains at the same level till the end of the measurement campaign.

The dynamic elastic moduli for NbTi conductors were calculated using formula (5). Figure 31 shows the dynamic elastic moduli upon increasing the load. The  $\partial\sigma_y/\partial\varepsilon_y$  are shown for cycle 30 000 except for the PF1&6 sample for which cycle 10 000 was chosen (the cycle before the bolts failure occurred). The evolution of  $\partial\sigma_y/\partial\varepsilon_y$  during the first cycle is shown only for the PFCN3 sample for clarity; the evolution of  $\partial\sigma_y/\partial\varepsilon_y$  during the first cycle for PFCN4 and MB samples are similar to the PFCN3 sample. The  $\partial\sigma_y/\partial\varepsilon_y$  of the PFCN3, PFCN4 and MB samples decreases from  $\sim 6 \text{ GPa}$  at zero load to around  $2 \text{ GPa}$  under full load at the first cycle. The evolution of  $\partial\sigma_y/\partial\varepsilon_y$  versus cycle number is less steep for NbTi conductors compared with Nb<sub>3</sub>Sn conductors. It takes 1,000 cycles for the PFCN3, PFCN4 and MB samples before  $\partial\sigma_y/\partial\varepsilon_y$  starts to follow the trajectory shown in figure 31. The dynamic elastic modulus of the CCCN3 sample stays at the level of  $1 \text{ GPa}$  during all loading cycles. The PF1&6 sample has the highest dynamic elastic modulus of  $\sim 7 \text{ GPa}$  at zero load increasing to  $\sim 11 \text{ GPa}$  at full load. At the first cycle, the PF1&6 sample showed a  $\partial\sigma_y/\partial\varepsilon_y$  of  $\sim 8 \text{ GPa}$  at zero load, decreasing to  $\sim 6 \text{ GPa}$  at full load. Upon decreasing load, the dynamic elastic moduli of all conductors behave in a similar way shown at figure 32.

### 3.7. Contact resistance measurements

Four samples were selected for contact resistance measurements: JAS-JA (TF type), PFCN3 (PF5 type), CS-JAS and CS-KAT (CS type) samples. The  $R_c$  between neighboring strands from the first cabling stage was monitored as a function of applied load while intra-petal and inter-petal resistances were measured only at zero and full load condition after a chosen number of cycles.



**Figure 25.** AC loss versus magnetic field frequency for the NbTi conductors in the initial state (left) and after 30 000 cycles (right).

**Table 8.** AC loss data on virgin state NiTi conductors.

Sample	$Q_{hys}$ (mJ/cycle cm <sup>3</sup> )		$n\tau$ (ms)	
	$B_a = \pm 0.15$ T	$B_a = 0.2-0.3$ T	$B_a = \pm 0.15$ T	$B_a = 0.2-0.3$ T
PFCN3	$7.3 \pm 0.1$	$3.4 \pm 0.1$	$136 \pm 10$	$96 \pm 10$
PFCN4	$7.5 \pm 0.1$	$3.9 \pm 0.1$	$82 \pm 3$	$49 \pm 3$
PF1&6	$9.9 \pm 0.1$	$4.7 \pm 0.1$	$211 \pm 11$	$209 \pm 11$
MB	$7.6 \pm 0.1$	$3.1 \pm 0.1$	$139 \pm 11$	$126 \pm 11$
CCCN3	$9.8 \pm 0.6$	$4.7 \pm 0.5$	$61 \pm 3$	$68 \pm 8$

**Table 9.** Measured properties of NbTi conductors.

		PFCN3	PFCN4	PF1&6	MB	CCCN3
$Q_{hys}$ (mJ/cycle cm <sup>3</sup> )	Initial state	$3.4 \pm 0.1$	$3.7 \pm 0.1$	$5.3 \pm 0.1$	$2.9 \pm 0.1$	$2.9 \pm 0.1$
	Final cycle	$3.4 \pm 0.1$	$3.4 \pm 0.1$	$5.3 \pm 0.1$	$3.0 \pm 0.1$	$2.7 \pm 0.1$
$n\tau$ (ms) initial state		$96 \pm 1$	$43 \pm 4^a$	$161 \pm 2$	$147 \pm 10$	$63 \pm 10^a$
	$n\tau$ (ms) final cycle					
$Q_m$ (mJ/cycle cm <sup>3</sup> )	Zero load	$123 \pm 1$	$94 \pm 2^a$	$178 \pm 1$	$242 \pm 1$	$128 \pm 1^a$
	Full load	$161 \pm 1$	$158 \pm 2^a$	$210 \pm 1$	$371 \pm 1$	$141 \pm 1^a$
	First cycle	57	60	13	43	2.7
	Final cycle	10	14	4 <sup>b</sup>	11	1.0
Final displacement ( $\mu$ m)		659	352	149	581	35
$E_y$ (GPa)	First cycle	2.2	2.8	7	1.7	2.5
	Final cycle	1.2	2.2	7 <sup>a</sup>	1.0	2.5

<sup>a</sup> Samples with low AC loss like PFCN4, or small volume like CC-type, require  $n\tau$  correction for the systematic error in the press setup. For the rest of the samples the correction is in the error bar of the experimental test and hence no correction is required.

<sup>b</sup> Measured at cycle 10 000.

### 3.7.1. Intra-triplet resistance as a function of applied load.

The intra-triplet  $R_c$  presented in this section is the average resistance over  $R_c$  values measured between strands from the first cabling stage that are specified in table 1. Figure 33 shows the typical evolution of the first cabling stage  $R_c$  versus applied load for the Nb<sub>3</sub>Sn conductors. The CS-JAS sample is taken as an example. The  $R_c$  curves show a clear hysteresis behavior during load–unload cycles. The  $R_c$  hysteresis loops are rather small at the initial cycles and are becoming more pronounced as the cycle number is increased (see figure 33). The overall  $R_c$  of the first cabling stage increases with inclining load cycle number. The CS-KAT sample and TF

sample JAS-JA show a similar evolution of the intra-triplet  $R_c$  versus applied load and cycle number.

The evolution of the intra-triplet  $R_c$  versus the applied load for NbTi conductors is shown in figure 34; the PFCN3 sample was taken as an example. The  $R_c$  curves versus applied load for NbTi conductors also show a hysteresis behavior during load–unload cycling. Hysteresis loops for NbTi conductors become less pronounced as the number of cycles is increased (see figure 34), which is opposite to Nb<sub>3</sub>Sn conductors. After 10 000 loading cycles a saturation seems reached and the  $R_c$  profile remains almost similar during cycling of the load.

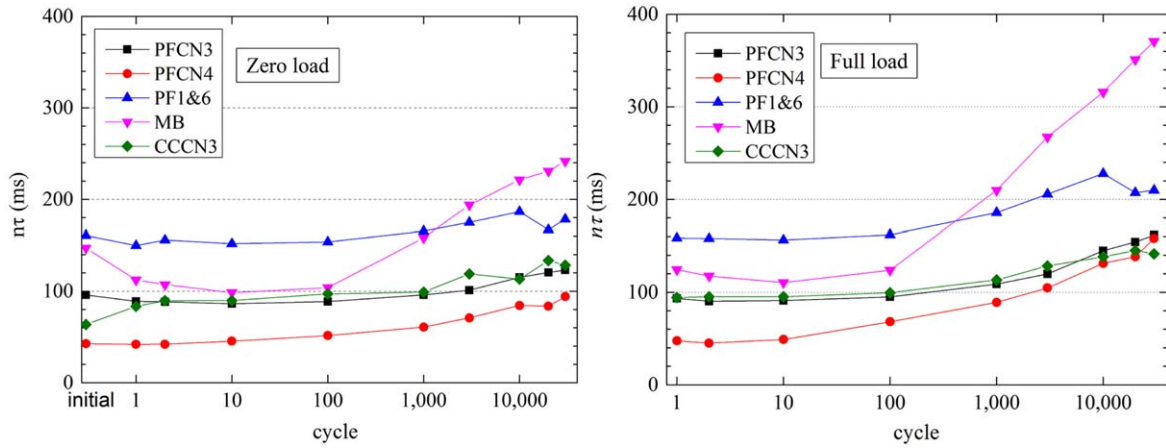


Figure 26. Evolution of  $n\tau$  values with cycles for fully loaded (right) and unloaded (left) states of the NbTi conductors.

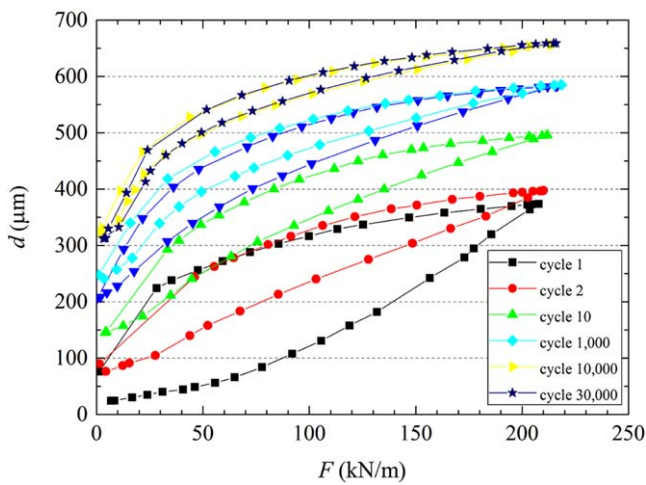


Figure 27. Typical force–displacement curves for an NbTi conductor at different cycles, the PFCN3 conductor is chosen here as an example.

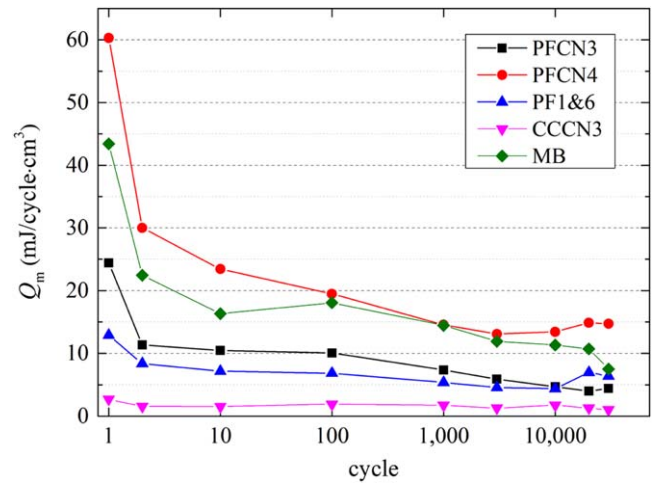


Figure 29. Evolution of the mechanical loss with load cycle for the NbTi conductors.

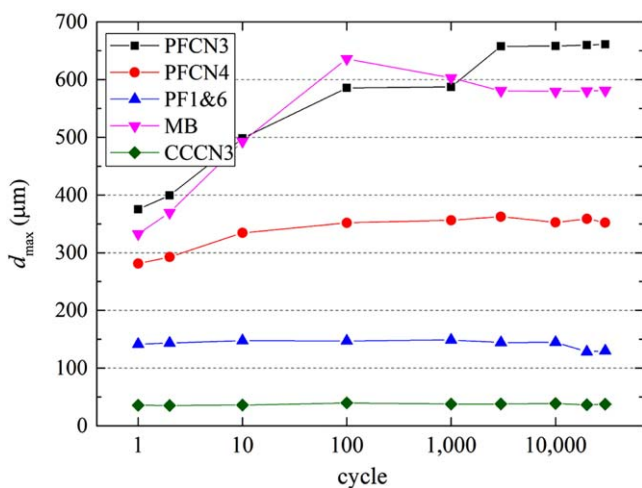


Figure 28. Evolution of displacement at maximum applied load with load cycle for NbTi conductors.

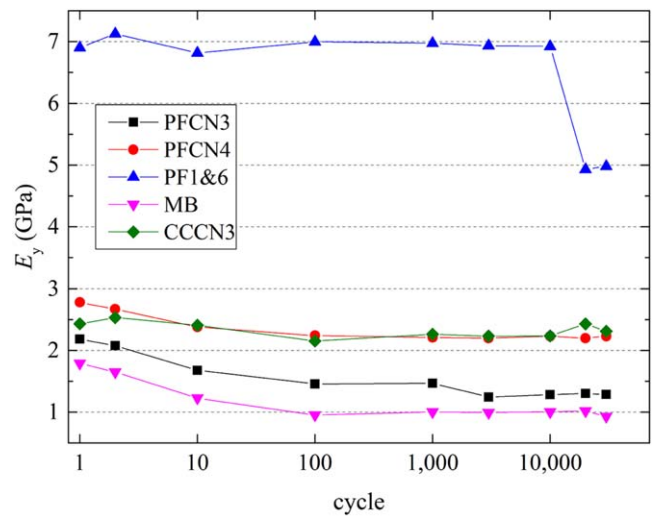


Figure 30. Evolution of the elastic moduli with cycle number for NbTi conductors.



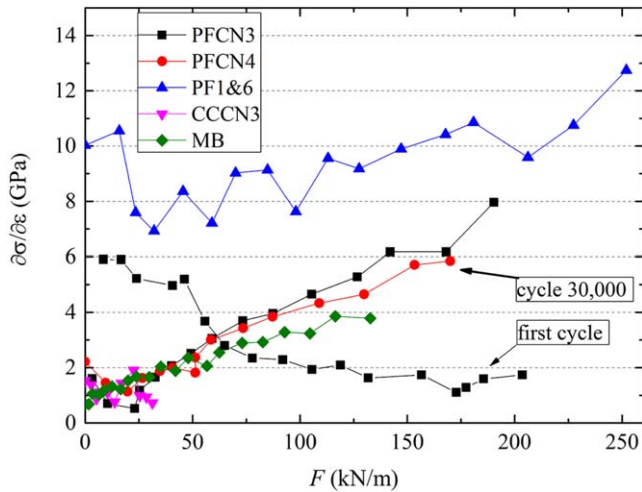


Figure 31. Dynamic elastic modulus upon increasing load for the NbTi conductors.

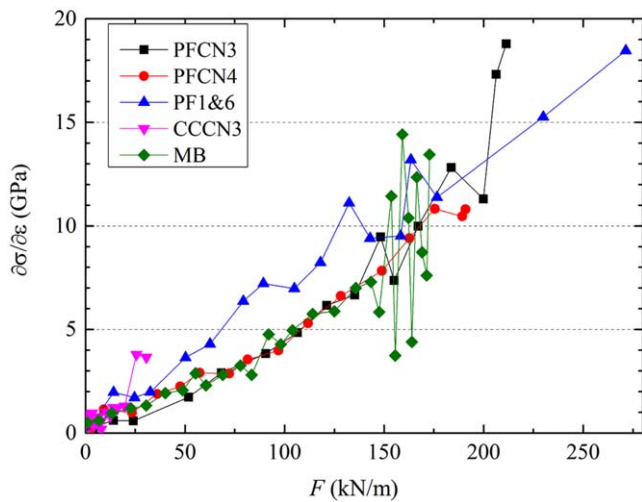


Figure 32. Dynamic elastic modulus upon decreasing load for the NbTi conductors.

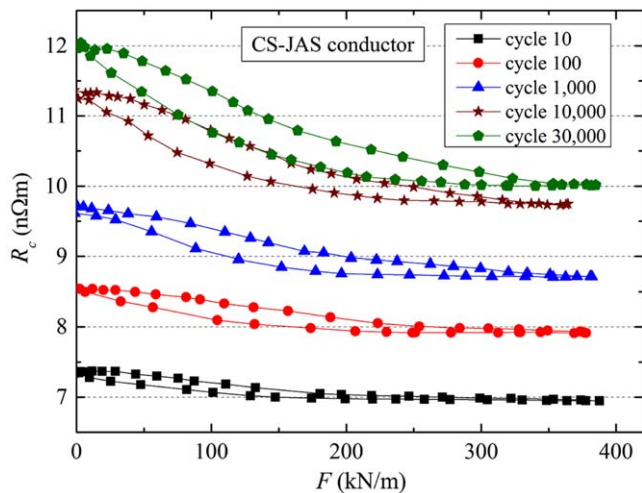


Figure 33. Typical evolution of the first cabling stage  $R_c$  versus the applied load. The  $R_c$  of the CS-JAS conductor shown at cycles 10, 100, 1,000, 10 000, and 30 000 is taken as an example.

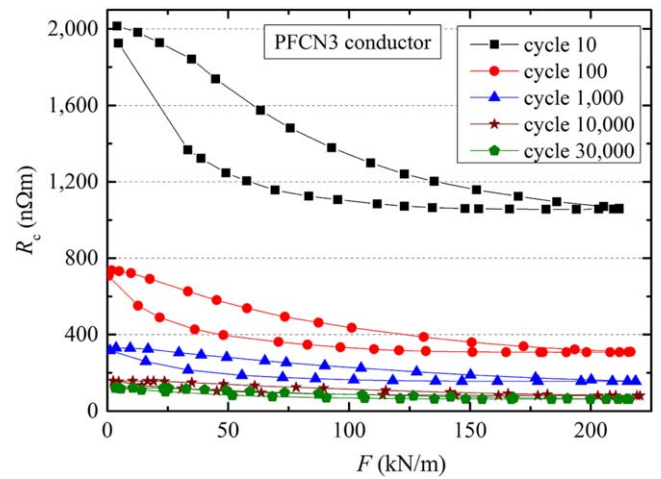


Figure 34. The  $R_c$  of the first cabling stage versus the applied load for the PFCN3 conductor at cycles 10, 100, 1000, 10 000, and 30 000.

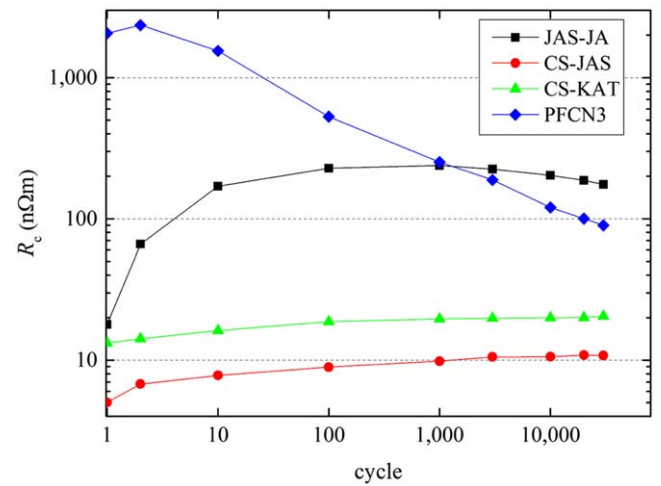
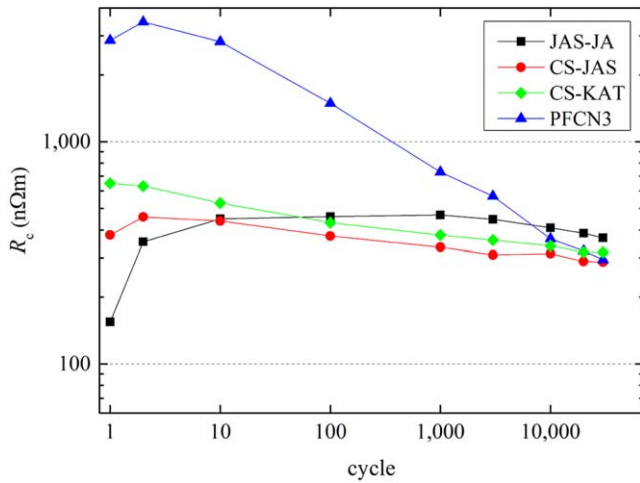


Figure 35. Average intra-petal  $R_c$  versus number of cycles at full load for JAS-JA, CS-KAT, JAS-JA and PFCN3 samples.

3.7.2. Contact resistance along load cycling. The intra-petal resistances  $R_c$  presented in this section are the average resistance value calculated over  $R_c$  measured between strand combinations specified in table 1. The average inter-petal  $R_c$  was calculated as an average  $R_c$  value measured between strands specified in table 2. As already shown in previous works on different conductor types [5, 11, 24], the  $R_c$  strongly depends on the applied load and on loading history on a methodical and qualitatively predictive way.

Table 10 presents the intra-petal resistances for the JAS-JA, CS-JAS, CS-KAT and PFCN3 samples at selected cycles for zero and full load while figure 35 shows the evolution of the  $R_c$  at full load as a function of loading cycles. The evolution of  $R_c$  versus cycle number at zero load has similar behavior while the absolute  $R_c$  values are higher compared with the fully loaded state.

Figure 36 shows a comparison of the average inter-petal  $R_c$  at full load as a function of cycle number for JAS-JA, CS-JAS, CS-KAT and PFCN3 samples. At first full load, the



**Figure 36.** Average inter-petal resistance versus cycle number for the TF-JAS, CS-JAS, CS-KAT and PFCN3 samples at full load.

Nb<sub>3</sub>Sn conductors have inter-petal resistances between 154 and 650 nΩ m. At cycle 10, the inter-petal  $R_c$  of all Nb<sub>3</sub>Sn conductors is about  $\sim 400$  nΩ m and then slowly decreases to  $\sim 300$  nΩ m at cycle 30 000. The PFCN3 sample has an inter-petal resistance of  $\sim 2850$  nΩ m at first full load. At cycle 2 the inter-petal  $R_c$  of the PFCN3 sample has a peak after which  $R_c$  gradually decreases to  $\sim 300$  nΩ m at cycle 30 000. Despite the difference in applied load and conductor type, all measured conductors show inter-petal  $R_c$  around 300 nΩ m after 30 000 loading cycles.

The general evolution of inter-petal  $R_c$  versus cycle number at zero load is similar to the behavior at full load but with higher  $R_c$  values.

## 4. Discussion

### 4.1. AC loss of TF conductors

For the coupling loss after cycling of the TF conductors in table 5, it appears that the OST-EU sample has rather exceptional high coupling loss. It is suggested that the rather exceptional high slope of the loss–frequency dependence of the OST-EU sample after cycling can be explained by accidental tin leakage occurred during the sample heat treatment. Inspection showed that tin leakage caused unintended soldering between a large number of strands and petal wraps at both ends of the sample. Figure 7 shows the loss–frequency dependence of the OST-EU sample without any corrections. It was suspected that there was additional AC loss due to tin leakage observed at the strand ends. The AC loss of the virgin OST sample was measured first with tin leak at the sample ends. After the first measurement, the sample ends with tin leak were removed by spark erosion and the AC loss measurement was repeated. The additional part of the coupling loss arisen due to the unintended soldering was about 105 mW. The  $nT$  values of the OST sample obtained from the press cyclic test then were corrected by subtraction of this factor.

In terms of  $Q_{hys}$ , the TF conductors can be separated in two groups. The first group includes the HIT-JA and JAS-JA conductors with  $Q_{hys} = 13.6 \pm 0.2$  and  $13.4 \pm 0.2$  mJ cm<sup>-3</sup> respectively. The second group includes the rest of TF samples with hysteresis losses spread between  $3.5 \pm 0.2$  mJ cm<sup>-3</sup> for BEAS (lowest) and  $7.03 \pm 0.2$  mJ cm<sup>-3</sup> for the WST-CN sample (highest in the second group). The groups can be clearly distinguished in figure 7(b) (and table 5) showing the loss–frequency dependence for samples after 30 000 cycles at zero load. The disparity in hysteresis loss values between TF conductors can be attributed to the difference in critical current density of strands from distinctive strand suppliers. The disparity in critical current density arises from the difference in strand cross-sectional layout (number and diameter of the filaments, processing technology and Cu/non Cu ratio) between different strand suppliers. This statement is supported by our results obtained with NbTi type conductors. We show in section 3.5 that conductors made from the same S2 type NbTi strands from the same supplier have similar hysteresis loss despite the difference in the conductor's layout.

From earlier work we know that there is a clear correlation between microscopic filament fracture, coupling and hysteresis loss in Nb<sub>3</sub>Sn strands [25]. Cracks reduce the effective filament diameter for hysteresis loss in internal tin type of strands due to breaking of the superconducting loops that were established by the bridging among Nb<sub>3</sub>Sn filaments. In ITER bronze type strand, longitudinal cracks in the filaments not only reduce the real filament dimensions but also the so-called effective filament diameter, which result in a decrease of hysteresis loss. The density and size of the longitudinal cracks increases with applied bending strain. The coupling loss also decreases with the growth of filament cracks, depending on the strand processing method. However, it appeared that the AC loss measurement sensitivity as a method to evaluate the number of cracks in an ITER Nb<sub>3</sub>Sn type CICC is relatively poor due to the small number of cracks after about 1000 electromagnetic loading cycles in the Sultan test facility [26]. Also in the press tests we observe some alterations in the conductors' hysteresis loss through load cycling that could possibly be caused by occurrence of undesired strand damage or filament breakages, leading to conductor performance degradation [21, 27–31].

For all samples, the change of the hysteresis loss manifests a decrease towards a lower value along with cycling. Most samples show a decrease of  $Q_{hys}$  between the initial state and the first cycle while no significant change of the hysteresis loss is observed after cycle 2. Figure 8(a) with a bronze processed BEAS-EU sample illustrates such a sudden drop of  $Q_{hys}$  at the first cycle. Only the KIS-KO sample showed a clear further reduction of the  $Q_{hys}$  after 3000 cycles as presented in figure 8(b). It should be noted that the change of hysteresis loss with cycling is small and mostly within or close to the error bar of the measurement. This can be expected according to [25] but the tendency is similar to that of the reduction of the current sharing temperature  $T_{cs}$  as observed in the SULTAN conductor tests [32].

**Table 10.** Average intra-petal resistances of measured samples at selected cycles.

$R_c$ (n $\Omega$ m)	Load	CS-JAS	CS-KAT	JAS-JA	PFCN3
Cycle 1	Initial state	5.2	12.2	11.3	1077.5
	Zero load	6.9	14.6	71.3	2988.8
	Full load	5.0	13.2	17.9	2060.0
Cycle 10	Zero load	8.2	17.3	321.3	2710.3
	Full load	7.8	16.2	169.6	1549.0
Cycle 100	Zero load	9.5	20.7	906.1	1259.3
	Full load	8.9	18.7	228.3	528.5
Cycle 1,000	Zero load	10.8	22.2	3151.9	521.6
	Full load	9.8	19.6	203.3	252.2
Cycle 30 000	Zero load	12.9	24.1	3471.2	170.4
	Full load	10.8	20.5	174.8	89.9

#### 4.2. Mechanical properties of TF conductors

All measured TF conductors display similar evolution of the displacement at maximum load versus cycle number, although at the first cycle, the conductor compaction differs. The conductors' absolute deformation increases further with cycling of the load. Compared with the first cycle, all TF conductors show a similar increase in the maximum displacement of  $360 \pm 60 \mu\text{m}$  after 30 000 loading cycles. An increase in the displacement rate was clearly observed for practically all TF conductors (except WST-CN and LUV-US samples) between cycles 10 000 and 30 000, see figure 11. The observed increase of the displacement rate after load cycling agrees with the evolution of single strand deformation as observed in measurements with the TARSIS contact stress probe [22]. This suggests that the evolution with cycling is mainly caused by strand deformation at strand's crossover contacts and in a less manner by bending of strands.

All conductors exhibit a similar evolution of  $E_y$  at maximum applied load as a function of cycle number, as shown in figure 13. Among the measured TF conductors, the JAS-JA and BEAS-EU conductors are the softest. It becomes clear that all conductors containing internal tin type of strands exhibit the highest  $E_y$ , while conductors with bronze processed strands have the lowest  $E_y$ , except for the CMP-RU. This is also well in agreement with the axial and transverse stiffness of the different strand types as measured in the TARSIS facility [22].

The dynamic  $E$ -modulus is a characteristic representing the change of the stiffness with increasing load. It shows the influence of the cable twist pattern on the cable deformation characteristics, besides the transverse stiffness and deformation properties of the Nb<sub>3</sub>Sn and softer copper strands. At low loads, a small value of the dynamic  $E$ -modulus represents a marginal impact of contact stress between crossing strands and the main deformation of strands in the cable is due to bending. The higher the force becomes, the closer the dynamic  $E$ -modulus approaches the strand transverse contact stiffness [22]. The larger the number of cycles at full cable load, the larger the strand deformation due to contact stress (pinching) becomes [22]. This is reflected by the continuous increase of deflection in figure 11. All these observations on

CICC's agree with the mechanical properties measured on strands [22].

Figure 12 shows that all measured TF conductors show very similar behavior of mechanical loss versus the number of load cycles. The mechanical loss is neglectable compared to the electromagnetic AC loss for ITER Plasma Scenario conditions.

Despite the different overall compression; the final stiffness is similar for most of the TF conductors and only WST-CN and LUV-US conductors exhibit a somewhat higher stiffness (see figure 15). The behavior of the dynamic elastic modulus correlates well with the change in the mechanical loss per cycle. Consequently, the WST-CN and LUV-US conductors with largest stiffness show the lowest mechanical losses among measured TF conductor samples.

#### 4.3. AC loss of CS conductors

Surprisingly, in spite of larger cable stiffness, a decrease of the hysteresis loss, just like in the TF conductors was observed for CS-JAS and to a lesser extent for the CS-KAT sample, although for CS conductors it is less likely to be caused by filament breakages during load cycling, it could be strain related since the current density depends on strain [25, 33]. Figure 18 shows the evolution of the  $Q_{hys}$  for the CS conductors with the number of loading cycles.

The CS conductors exhibit gradual  $n\tau$  decay with cycle number unlike the fast decrease of  $n\tau$  within the first ten cycles as observed for TF conductors, see figures 9 and 19. The difference between CS and TF conductors in evolution of the coupling loss with cyclic load is explained by the difference in stiffness due to the selected cable pattern. The CS conductors use a short twist pitch scheme, which means that the strands have less space for bending and movement compared to the TF conductors. Short twist pitch restricts strand movement hence preserving the low resistive contacts between strands formed during conductor heat treatment. This results in a smoother evolution of the coupling loss versus cycle number. A similar evolution of the coupling loss under cyclic load was observed for a TF prototype conductor with low void fraction, also creating limited strand movement [20]. Surprisingly, in spite of larger cable stiffness, a decrease of



the hysteresis loss, just like in the TF conductors, was observed in CS-JAS and to a lesser extent in the CS-KAT sample, although for CS conductors it is less likely to be caused by filament breakages during load cycling [26].

#### 4.4. Mechanical properties of CS conductors

The short twist pitch scheme of the CS conductors provides the strands more support and less space for bending and movement compared with TF conductors. The higher tightness results in increased transverse stiffness resulting in lower mechanical losses of CS conductors compared with TF conductors. The shape of the displacement-force curves of the CS conductors are similar to those observed on TF conductors (figure 10) but with a smaller displacement at maximum load and smaller hysteresis loop.

The CS-JAS sample, made of softer bronze type strands, has a larger deflection than the CS-KAT sample with stiffer internal tin type of strands. As mentioned above, it was shown in previous work on ITER Nb<sub>3</sub>Sn strands with use of the TARSIS facility that bronze strands are softer for axial loading and bending than internal tin type [34].

#### 4.5. AC loss of NbTi CICC

The NbTi conductor's AC loss can be separated into two groups by  $Q_{hys}$  values, as shown in figure 25. The first group of conductors, with a  $Q_{hys}$  of about  $3.2 \pm 0.3 \text{ mJ cm}^{-3}$  includes PFCN3, PFCN4, MB and CCCN3 samples. The PF1&6 sample have a higher  $Q_{hys}$  of  $5.3 \pm 0.1 \text{ mJ cm}^{-3}$ . The difference in  $Q_{hys}$  is related to the difference in NbTi strands that is used in PF1&6 and the rest of the NbTi conductors. The PF1&6 conductor designed for higher peak load uses strand type S1 while strand type S2 are used in the rest the conductors (PFCN3, PFCN4, MB, CCCN3). The measured  $Q_{hys}$  is in agreement with the technical requirements for ITER strand; the  $Q_{hys}$  for S1 type of strand is foreseen to be higher ( $<55 \text{ mJ cm}^{-3}$ ) than for S2 type of strand ( $<45 \text{ mJ cm}^{-3}$ ) [2, 35]. It is indeed observed here that conductors made out of the same S2 type NbTi strands have similar  $Q_{hys}$ . The PF1&6 sample made out of S1 type strand with lower Cu/non Cu ratio 1.65 has substantially higher  $Q_{hys}$ .

The  $Q_{hys}$  of the NbTi conductors remains at the same level before, during and after the cycling test (see table 9), in contrast to the Nb<sub>3</sub>Sn TF and CS conductors, emphasizing the distinctive role of the filaments strain and breakage during load cycling in the Nb<sub>3</sub>Sn type of conductors. This confirms that the relatively large decrease in hysteresis loss as observed with the Nb<sub>3</sub>Sn TF and even CS conductors, is an artifact of filament strain changes or even damage, understandably not occurring in NbTi type of strands. It also confirms that the observed changes of  $Q_{hys}$  with cycling in CS and TF CICC is highly unlikely related to an experimental error.

The  $n\tau$  evolution with cycle number shown in see figure 26, is qualitatively different between NbTi and Nb<sub>3</sub>Sn conductors. The initial  $n\tau$  values of the NbTi conductors varies from  $\sim 45 \text{ ms}$  for the PFCN4 sample to  $\sim 161 \text{ ms}$  for the PF1&6 sample. When the cycling load is started, the  $n\tau$

values of the NbTi conductors slightly decrease or stay at the same level until cycle 100, after which they start to rise. The rate of  $n\tau$  increase is highest for the MB conductor. This can be explained by the absence of stainless steel wraps around the petals in the MB conductor, since all other conductors have wraps around their petals. Similar fast increase of coupling loss with cycling load was observed earlier on an NbTi CICC, e.g. on the PFIS conductor without petal wraps [24]. It was previously shown that for a conductor without petal wraps, the last stage inter-petal coupling loss is dominant, in particular at the low frequency range [24]. The absence of petal wraps in the MB conductor leads to a significant effective decrease in the inter-petal resistance and results in increased coupling loss. The increase of  $n\tau$  values observed for the rest of the NbTi conductors is much smaller (see figure 26).

#### 4.6. Mechanical properties of NbTi conductors

When the displacement versus force curves of NbTi conductors (figure 27) are compared with Nb<sub>3</sub>Sn conductors (figure 10), it is clear that the NbTi conductors show a higher rate of conductor relaxation during force release and smaller permanent deformation. This can be attributed to the higher stiffness and lower degree of plastic deformation of NbTi strands.

The mechanical loss in NbTi conductors, shown in figure 29, decreases more gradual compared with Nb<sub>3</sub>Sn conductors (figure 12) and depends strongly on the peak load and conductor layout. The PF1&6 sample that uses only NbTi strands without co-twisted copper strands, has the lowest mechanical loss among the PF type of conductors while the peak load for the PF1&6 is the highest among the measured NbTi conductors. The gradual decrease of the mechanical loss for the PF1&6 sample represents the deformation of NbTi strands only while the rest of conductors has co-twisted copper strands and work hardening of the copper strands under repeated cycling load is also playing a role during the first cycles.

The effective elastic moduli of all NbTi samples, except PF1&6, decrease slightly within the first 100 cycles and remains at the same level till the end of the measurement campaign (figure 30). The PF1&6 sample's effective elastic modulus stays at the level of 7 GPa till cycle 10 000. The high elastic modulus of the PF1&6 sample can be explained by the low void fraction of the PF1&6 conductor and absence of co-twisted copper strands. The S1 type strands used in the PF1&6 conductor also have lower Cu/non Cu ratio of 1.65 compared with the 2.35 ratio of the S2 type strands, that makes the PF1&6 sample the stiffest among the measured NbTi conductors. The sharp decrease of the PF1&6 sample's elastic modulus between cycle 10 000 and 20 000 is explained by breakage of two out of 12 bolts securing the initial void fraction of the sample and subsequent sample expansion in transverse direction by  $\sim 74 \mu\text{m}$  in average. The forces on the bolts were high in this case due to internal residual stresses in the conduit material, being transferred to the bolts.



#### 4.7. Contact resistance

As shown in figure 35, the qualitative behavior of the intra-petal  $R_c$  obtained on all Nb<sub>3</sub>Sn conductors is similar, ensuing an increase of  $R_c$  with the number of loading cycles. However, the resistance of the CS-KAT conductor stays about twice as high as the CS-JAS sample along cycling, see table 10. The short twist pitch structure leads to a tightly packed structure of the cable that restricts strands movement, which in turn preserve the low resistive contacts that are formed during heat treatment. That results in a relatively small change of  $R_c$  for CS conductors during cycling of the load. The JAS-JA sample (TF type) shows a much larger change in contact resistance with cycling compared to CS conductors. The intra-petal  $R_c$  of the JAS-JA sample increases by an order of magnitude at full load and by two orders of magnitude at zero load within the first 100 cycles, see table 10. After 3000 cycles a small decrease of the  $R_c$  measured under full load is observed, while the  $R_c$  values measured at zero load are still slightly rising.

The intra-petal  $R_c$  of the NbTi PFCN3 conductor has dissimilar evolution, which is well in agreement with previous observations [5]. The initial intra-petal resistance is two orders of magnitude higher than those of Nb<sub>3</sub>Sn conductors, see table 10. When cyclic loading is started, the  $R_c$  increases slightly and reaches a maximum at the second cycle of  $\sim 2000$  n $\Omega$  m at full load and  $\sim 3000$  n $\Omega$  m at zero load. After the second cycle, the intra-petal  $R_c$  of the PFCN3 sample starts to decrease gradually with cycling, reaching eventually 90 n $\Omega$  m at full load and 170 n $\Omega$  m at zero load after 30 000 cycles. The decrease of contact resistance in NbTi conductors is associated with polishing and wearing of the oxide layer and reduction of the surface strand roughness. A NbTi prototype PF conductor with strands having a Cr coating, like Nb<sub>3</sub>Sn conductors, also showed a similar decrease of contact resistance with cycling load [5]. At the same time, Nb<sub>3</sub>Sn conductors with Cr coated strands and subjected to a heat treatment in vacuum or inert gas show a strong increase of contact resistance with cycling load, even when being subjected to higher transverse load. The relation between contact resistance and thickness of the oxidation layer was investigated and confirmed in [36, 37].

For the PFCN3, CS-JAS and CS-KAT samples, the order of cabling stage corresponds well with the sequence of the measured contact resistance values. The lowest intra-petal  $R_c$  is observed for the first cabling stage as its strands are most tightly twisted with direct line contact while the highest  $R_c$  value is observed for the strands between the fourth cabling stages. The TF JAS-JA sample did not show such correlation between cabling stage and resistance.

#### 4.8. Correlation between contact resistance and coupling loss

In previous studies [5], an empirical relation was formulated between the conductor's coupling loss time constant and its inter-strand contact resistance. The relation can be expressed

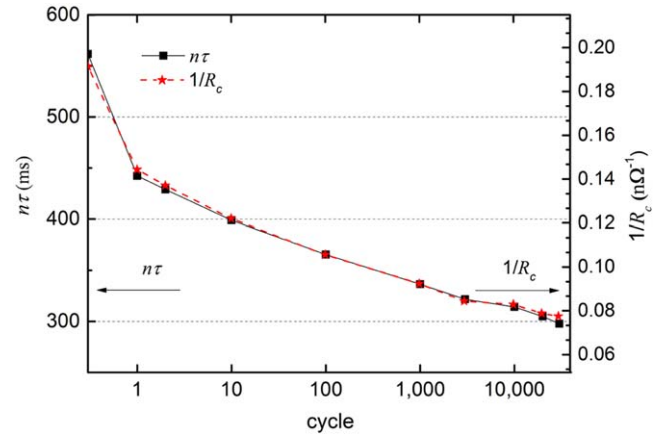


**Figure 37.** Coupling loss time constant and  $1/R_c$  evolution as a function of cycle number for the CS-JAS sample.

as follows:

$$n\tau_{\text{tot}} = \frac{\beta_1}{R_c^1} + \frac{\beta_2 L_{p2}^2 D_2^2}{R_c^2} + \frac{\beta_3 L_{p3}^2 D_3^2}{R_c^3} + n\tau_{\text{strand}} \quad (\text{S}), \quad (5)$$

where  $\beta$  is a fitting constant,  $L_p$  is the twist pitch length of the corresponding cable stage,  $D$  is the diameter of the considered cable element, the index 1 is referring to the first triplet cabling stage, index 2 to the sub-petal cabling stage and index 3 to the last cabling stage,  $n\tau_{\text{strand}}$  represents the intra-strand coupling loss. Here we consider only the correlation between the first triplet  $R_c$  and the coupling loss time constant, neglecting sub-petal and last cabling stages as well as the intra-strand coupling loss. Figure 37 shows the correlation between the evolution of the coupling loss time constant  $n\tau$  and the first triplet's average  $1/R_c$  versus cycle number at fully unloaded state. The good correlation between  $n\tau$  and first triplet  $1/R_c$  is observed for all measured conductors JAS-JA, CS-KAT, CS-JAS, and PFCN3 for zero as well as for full load state. However, the fitting parameter  $\beta_1$  is unique for each conductor. Though the AC coupling loss is measured only at zero and full load, the good correlation between intra-petal resistance and coupling loss time constant gives confidence for the likelihood of an accurate estimate of the coupling loss under a fraction of the load with using  $R_c(F)$  data that was measured for the first triplet.

#### 4.9. Comments

The tests results obtained on TF, CS and PF ITER conductors in the Twente Cryogenic Cable Press show distinctive conduct in deformation, which is characteristic for their cabling pattern, void fraction and strand material; Nb<sub>3</sub>Sn and NbTi. The overall tendency and the prominent role of the mentioned conductor design specifications, as already predicted and pointed out in 2006 [38, 39] gives a clear guideline for future conductor design as far as the mechanical properties related to transverse load optimization are concerned. Strand movement for fragile material like Nb<sub>3</sub>Sn in cabled conductors being subjected to large transverse loads, should be avoided. Although different solutions for this are feasible, the

associated cable patterns are understandably directly linked to the level of coupling loss that is generated in transient applied magnetic fields. Recently proposed cable patterns, addressing the minimization of coupling losses in combination with maximum lateral strand support against transverse load, are under investigation for the next generation of fusion conductors [12, 40]. For ITER, the proven design solutions from [38], tested in 2008 [39], were only partly implemented in the ITER TF conductor, resulting in still relatively poor performance and degradation with cycling. However, the fraction of filament breakage was severely restricted [22] by increasing the cable twist pitches and main part of the transverse load degradation during cycling in ITER TF is attributed to strand periodic bending inducing filament strain variations.

The higher transverse stiffness of the CS Nb<sub>3</sub>Sn conductors compared to that of the TF conductors leads to better performance with load cycling, which has been confirmed by Sultan and Insert Coil tests. The cable pattern of the ITER CS is based on the so-called short twist pitch design, also proposed as an optimized variant in [38].

Both ITER conductor designs, TF and CS are not optimized for coupling loss, and only the CS is robust against transverse load degradation. The advantage of coupling loss reduction with cycling, as observed for the press tests, becomes significantly less pronounced when the stiffness of the cable increases, since strands have less freedom to move in that case and the inter-strand contact resistance remains on a fairly low level. So, improving the cable stiffness must be accompanied by optimization of the cable pattern towards lower coupling loss. The ITER PF NbTi conductors do not suffer from transverse load degradation since their performance is not sensitive to strain. Thus, optimization of the cable pattern essentially seems only relevant for reduction of the coupling loss. The Press observations clearly demonstrate an increase of the coupling loss with cycling for the NbTi CICC's. The higher coupling loss is due to a decrease of inter-strand contact resistance in NbTi conductors, which on its turn is probable associated with polishing and wearing of the oxide layer and reduction of the strand surface roughness. In particular this phenomenon of wearing could be a endorsed reason to improve as well the stiffness of the NbTi conductors for future fusion reactors in order to exclude the increase of coupling loss with cycling.

## 5. Summary

All types of CICC's being used in ITER magnet coils were subjected to transverse cyclic loading up to 30 000 loading cycles. The applied load in the Twente Cryogenic Cable Press simulates the Lorentz forces during magnet operation. It is shown that cyclic load has a strong influence on the conductors' electrical and mechanical properties. The evolution of the AC losses, contact resistances and mechanical properties with load cycling was studied for eight TF, two CS, three PF conductors of different types (PF1&6, PF4, PF5), one MB and one CC conductor.

Eight TF conductors produced by different domestic manufacturers were tested under identical conditions. The coupling loss time constant of the TF conductors in the initial state varies from  $360 \pm 10$  to  $1220 \pm 30$  ms. All TF conductors, except one, showed a similar evolution of the coupling loss with cyclic loading. The coupling loss time constant  $n\tau$  decreases fast within the first ten cycles and saturates after cycle 100. Under full load, two  $n\tau$  saturation levels are observed, one around 100 ms and another of about 180 ms. One TF sample showed rather gradual  $n\tau$  decrease compared with the rest of TF conductors with a saturation level of 267 ms at full load. All measured TF conductors show very similar behavior for the evolution of mechanical properties versus load cycles. During the first cycle, the mechanical loss of the TF conductors varies from 264 to 416 mJ/cycle cm<sup>3</sup>. At the second cycle, all TF conductors showed a mechanical loss less than 100 mJ/cycle cm<sup>3</sup> while the saturation level of  $\sim 20$  mJ/cycle cm<sup>3</sup> is reached at cycle 100 for all conductors. All TF conductors also exhibit a similar evolution of the displacement, elastic modules and stiffness with load cycles.

The impact of cycling load on Central Solenoid conductors is less pronounced due to the tighter structure of the strand bundle. The AC coupling loss decays only very modest with cycling of the load and even after 30 000 load cycles no saturation was reached. At cycle 30 000 the  $n\tau$  value remains at rather high level of 363 ms at full load for the CS-JAS sample and 179 ms for the CS-KAT conductor.

The CS conductor made of softer bronze type of strands has a larger deflection and higher mechanical loss at first cycle compared to the CS conductor that is made of stiffer internal tin type of strands. Nevertheless, after ten load cycles the change in mechanical properties of both CS samples becomes similar. Both conductors reach the same saturation level in mechanical loss of  $\sim 13$  mJ/cycle cm<sup>3</sup> and deformation rate. Compared with Nb<sub>3</sub>Sn conductors, the mechanical loss of NbTi conductors has lower initial level and at the same time a more gradual decrease rate.

A correlation is observed between the reduction of the hysteresis loss with cycling and the possible influence of filament strain or damage in conductors containing Nb<sub>3</sub>Sn strands. This is confirmed by the clear difference in performance between Nb<sub>3</sub>Sn and NbTi CICC's, showing only reduction of the hysteresis loss for the Nb<sub>3</sub>Sn type of CICC's. Although the sensitivity of the used method is poor for quantitative analysis of the fraction of filaments damaged volume, the characteristic behavior of the hysteresis loss with load cycling seems in line with the degradation of the current sharing temperature of the TF conductors during qualification tests, with the largest decrease during the first load.

The NbTi conductors subjected to cycling load show a small decrease of the coupling loss during the first 10 cycles, after which the coupling loss time constant starts to increase although staying within likely tolerable limits of around 200 ms up to 30 000 cycles. The increase rate is about the same for all measured NbTi conductors except for the MB conductor as a consequence of its different cable layout.

A TF, PF and two CS samples were chosen for contact resistance measurements during cycling of the load. The Nb<sub>3</sub>Sn conductors show a similar evolution of the intra-petal contact resistance with initially low values that increase upon load cycling. The NbTi conductor shows an opposite behavior of the intra-petal contact resistance with initially relatively high contact resistances, which decrease upon load cycling. All samples show a good correlation between the evolution of the coupling loss time constant and average contact resistance of the first triplet.

## Disclaimer

The views and opinions expressed herein do not necessarily reflect those of the ITER Organization.

## ORCID iDs

K A Yagotintsev  <https://orcid.org/0000-0002-4354-3959>

A Nijhuis  <https://orcid.org/0000-0002-1600-9451>

## References

- [1] Mitchell N, Bessette D, Gallix R, Jong C, Knaster J, Libeyre P, Sborchia C and Simon F 2008 The ITER magnet system *IEEE Trans. Appl. Supercond.* **18** 435
- [2] Devred A, Backbier I, Bessette D, Bevilard G, Gardner M, Jewell M, Mitchell N, Pong I and Vostner A 2012 Status of ITER conductor development and production *IEEE Trans. Appl. Supercond.* **22** 4804909
- [3] Hamada K, Takahashi Y, Matsui K, Kato T and Okuno K 2004 Effect of electromagnetic force on the pressure drop and coupling loss of a cable-in-conduit conductor *Cryogenics* **44** 45
- [4] Nijhuis A and Ilyin Y 2009 Transverse cable stiffness and mechanical losses associated with load cycles in ITER Nb<sub>3</sub>Sn and NbTi CICC *Supercond. Sci. Technol.* **22** 055007
- [5] Nijhuis A, Yu I, Abbas W, Haken ten B and ten Kate H H J 2004 Change of interstrand contact resistance and coupling loss in various prototype ITER NbTi conductors with transverse loading in the Twente cryogenic cable press up to 40 000 cycles *Cryogenics* **44** 319
- [6] Nijhuis A, Noordman N, ten Kate H, Mitchell N and Bruzzone P 1998 Magnetic and mechanical AC loss of the ITER CS1 model coil conductor under transverse cyclic loading *Physica C* **310** 253–7
- [7] Fuchs A, Blau B, Bruzzone P, Vecsey G and Vogel M 2001 Facility status and results on ITER full-size conductor tests in SULTAN *IEEE Trans. Appl. Supercond.* **11** 2022–5
- [8] Bruzzone P *et al* 2008 Results of a new generation of ITER TF conductor samples in SULTAN *IEEE Trans. Appl. Supercond.* **18** 459–62
- [9] Bruzzone P, Stepanov B, Wesche R, Calzolaio C, March S and Vogel M 2012 Operation and test results from the SULTAN test facility *IEEE Trans. Appl. Supercond.* **22** 9501704
- [10] Bruzzone P *et al* 2012 Test results of ITER conductors in the SULTAN facility *Proc. 24th IAEA Fusion Energy Conf. (San Diego, USA, 8–13 October 2012)*
- [11] Miyoshi Y, Ilyin Y, Abbas W and Nijhuis A 2011 AC loss, inter-strand resistance, and mechanical properties of an option-II ITER CICC up to 30 000 cycles in the press *IEEE Trans. Appl. Supercond.* **21** 1944–7
- [12] Nijhuis A, van Lanen E P A and Rolando G 2012 Optimization of ITER Nb<sub>3</sub>Sn CICC for coupling loss, transverse electromagnetic load and axial thermal contraction *Supercond. Sci. Technol.* **25** 015007
- [13] Rolando G, van Lanen E P A and Nijhuis A 2012 Minimum quench power dissipation and current non-uniformity in international thermonuclear experimental reactor type NbTi cable-inconduit conductor samples under direct current conditions *J. Appl. Phys.* **111** 093904
- [14] Nijhuis A 2012 Comparison between evolution of Twente Press AC loss (2005) and PF coil insert (2008) on similar PF conductor (PFCl) *Oral presentation at SWG Meeting, SULTAN Test Review & SWG Meetings (CRPP, Villigen, 26–28 March)* (unpublished)
- [15] Abbas W, Nijhuis A, Yu I, ten Haken B and ten Kate H H J 2004 A fully automatic press for mechanical and electrical testing of fullsize ITER conductors under transverse cyclic load *AIP Conf. Proc.* **711** 51
- [16] Nijhuis A, Noordman N H W and ten Kate H H J 1997 800 kN press for mechanical and electrical testing of full-size ITER cables under transverse loading *Intermediate Report 1, 2 and 3 UT-NET 97-1, NET Contract No. 95/389* University of Twente
- [17] Nijhuis A, Noordman N H W, ten Kate H H J, Mitchell N and Bruzzone P 1998 A press for mechanical and electrical testing of fullsize ITER conductors under transverse loading *MT-15 Proc.* (Beijing: Science Press) p 441
- [18] Nijhuis A, Noordman N, Shevchenko O and ten Kate H 1999 Electromagnetic and mechanical characterisation of ITER CS-MC conductors affected by transverse cyclic loading: III. Mechanical properties *IEEE Trans. Appl. Supercond.* **9** 165
- [19] Takahashi Y, Matsui K, Nishii K, Koizumi N, Nunoya Y, Isono T, Ando T, Tsuji H, Murase S and Shimamoto S 2001 AC loss measurement of 46 kA-13 T Nb<sub>3</sub>Sn conductor for ITER *IEEE Trans. Appl. Supercond.* **11** 1546–9
- [20] Nijhuis A, Yu I, Abbas W, ten Kate H, Ricci M and della Corte A 2005 Impact of void fraction on mechanical properties and evolution of coupling loss in ITER Nb<sub>3</sub>Sn conductors under cyclic loading *IEEE Trans. Appl. Supercond.* **15** 1633
- [21] Nijhuis A, ten Kate H, Bruzzone P and Bottura L 1996 Parametric study on coupling loss in subsized ITER Nb<sub>3</sub>Sn cabled specimen *IEEE Trans. Magn.* **32** 2743
- [22] Nijhuis A *et al* 2013 The effect of axial and transverse loading on the transport properties of ITER Nb<sub>3</sub>Sn strands *Supercond. Sci. Technol.* **26** 084004
- [23] Kwon S P, Sim K-H, Ma Y J, Park S-H, Park P-Y, Shin I-S, Choi H, Seo Y-H, Jang K-H and Park W 2015 Prototype Nb<sub>3</sub>Sn superconducting strand for ITER CS coil conductor produced in Korea using the internal-tin route *IEEE Trans. Appl. Supercond.* **25** 4201106
- [24] Ilyin Y, Nijhuis A, Abbas W, Bruzzone P, Stepanov B, Muzzi L, Gislou P and Zani L 2005 Effect of cyclic loading and conductor layout on contact resistance of full-size ITER PFCl conductors *IEEE Trans. Appl. Supercond.* **15** 1359
- [25] Zhou C, Bink D, Liu B, Miyoshi Y, Wessel W A J, Krooshoop H J G and Nijhuis A 2012 Magnetization measurements on ITER Nb<sub>3</sub>Sn CICC and strands subjected to irreversible strain degradation *Supercond. Sci. Technol.* **25** 075004
- [26] Sanabria C, Lee P, Starch W, Pong I, Vostner A, Jewell M, Devred A and Larbalestier D 2012 Evidence that filament fracture occurs in an ITER toroidal field conductor after cyclic Lorentz force loading in SULTAN *Supercond. Sci. Technol.* **25** 075007

- [27] Ekin J W 1981 *Superconducting Materials Science—Metallurgy, Fabrication and Applications* (New York: Plenum)
- [28] Mitchell N 2003 *Fusion Eng. Des.* **66–68** 971–93
- [29] Ekin J W 1984 *Adv. Cryog. Eng.* **30** 823–36
- [30] Miyoshi Y, van Lanen E P A, Dhalle M and Nijhuis A 2009 Distinct voltage–current characteristics of Nb<sub>3</sub>Sn strands with dispersed and collective crack distributions *Supercond. Sci. Technol.* **22** 0953–2048
- [31] Jewell M C, Lee P J and Larbalestier D C 2003 The influence of Nb<sub>3</sub>Sn strand geometry on filament breakage under bend strain as revealed by metallography *Supercond. Sci. Technol.* **16** 1005–11
- [32] Devred A, Backbier I, Bessette D, Bevillard G, Gardner M, Jong C, Lillaz F, Mitchell N, Romano G and Vostner A 2014 Challenges and status of ITER conductor production *Supercond. Sci. Technol.* **7** 044001
- [33] Sanabria C, Lee P J, Starch W, Devred A and Larbalestier D C 2015 Metallographic autopsies of full-scale ITER prototype cable-in-conduit conductors after full cyclic testing in SULTAN: II. Significant reduction of strand movement and strand damage in short twist pitch CICC's *Supercond. Sci. Technol.* **28** 125003
- [34] van den Eijnden N C, Nijhuis A, Ilyin Y, Wessel W A J and ten Kate H H J 2005 Axial tensile stress–strain characterization of ITER model coil type Nb<sub>3</sub>Sn strands in TARSIS *Supercond. Sci. Technol.* **18** 1–10
- [35] Liu W, Liu X, Feng Y, Xie H, Wang T and Li J 2010 Development of fine filament NbTi superconducting strands for ITER *IEEE Trans. Appl. Supercond.* **20** 1504
- [36] Nijhuis A and ten Kate H 2000 Surface oxidation and interstrand contact resistance of bare and Cr-coated Nb<sub>3</sub>Sn and NbTi strand material in CICC's *Adv. Cryog. Eng. (Materials)* **46** 1083
- [37] Nijhuis A, ten Kate H, Pantsyrny V, Shikov A and Santini M 2000 Interstrand contact resistance and AC loss of a 48-strands Nb<sub>3</sub>Sn CIC conductor with a Cr/Cr-oxide coating *IEEE Trans. Appl. Supercond.* **10** 1090
- [38] Nijhuis A and Ilyin Y 2006 Transverse load optimisation in Nb<sub>3</sub>Sn CICC design; influence of cabling, void fraction and strand stiffness *Supercond. Sci. Technol.* **19** 945–62
- [39] Nijhuis A 2008 A solution for transverse load degradation in ITER Nb<sub>3</sub>Sn CICC's: verification of cabling effect on Lorentz force response *Supercond. Sci. Technol.* **21** 054011
- [40] Rolando G, Devred A and Nijhuis A 2014 Minimizing coupling loss by selection of twist pitch lengths in multi-stage cable-in-conduit conductors *Supercond. Sci. Technol.* **27** 015006